Icarus 226 (2013) 999–1019

Contents lists available at ScienceDirect

Icarus

journal homepage: www.elsevier.com/locate/icarus

The inner small satellites of Saturn: A variety of worlds

P.C. Thomas [a,*], J.A. Burns [a], M. Hedman [a], P. Helfenstein [a], S. Morrison [b], M.S. Tiscareno [a], J. Veverka [a]

[a] Center for Radiophysics and Space Research, Cornell University, Ithaca, NY 14853, USA
[b] Department of Planetary Sciences, University of Arizona, Tucson, AZ 85721, USA

ARTICLE INFO

Article history:
Received 22 March 2013
Revised 10 July 2013
Accepted 13 July 2013
Available online 22 July 2013

Keywords:
Saturn, Satellites
Geological processes
Geophysics
Photometry

ABSTRACT

More than a dozen small (<150 km mean radius) satellites occupy distinct dynamical positions extending from within Saturn's classical rings to the orbit of Dione. The Cassini mission has gradually accumulated image and spectral coverage of these objects to the point where some generalizations on surface morphology may be made. Objects in different dynamical niches have different surface morphologies. Satellites within the main rings display equatorial ridges. The F-ring shepherding satellites show structural forms and heavily cratered surfaces. The co-orbitals Janus and Epimetheus are the most lunar-like of the small satellites. Satellites occupying libration zones (Trojan satellites) have deep covering of debris subject to downslope transport. Small satellites embedded in ring arcs are distinctively smooth ellipsoids that are unique among small, well-observed Solar System bodies and are probably relaxed, effectively fluid equilibrium shapes indicative of mean densities of about 300 kg m^{-3}.

1. Introduction

The smaller (<150 km mean radius) satellites of Saturn occupy several dynamical niches: associated with rings (Pan, Daphnis, Atlas, Prometheus, Pandora), co-orbiting between the F ring and the larger satellites (Janus and Epimetheus), orbiting in faint rings or in ring arcs (Aegaeon, Methone, Anthe, Pallene), and orbiting libration points of larger moons (Telesto, Calypso, Polydeuces, and Helene). Hyperion, the largest irregularly-shaped satellite of Saturn, orbits between Titan and Iapetus, and Phoebe, the next largest, is in a retrograde orbit well outside the orbits of the large satellites. Many smaller objects orbit farther from Saturn (Gladman et al., 2001; Denk et al., 2011); they are not resolved in Cassini images and are not considered in this work.

The small satellites do not experience the internally driven processes that larger objects do, but the imaging survey by Cassini has shown distinct differences in morphology among the small objects that vary with their orbital and dynamical groupings. This correlation suggests that their morphologies, shaped by external rather than internal processes, may reveal aspects of the dynamics of materials orbiting close to Saturn. This work examines the morphological characteristics of these satellites and outlines some of the possible mechanisms that may explain the variations among objects that do not suffer effects of internal activity.

The small satellites generally are expected to be fragments or rubble-like assemblages. The higher-density example of Phoebe may be an exception (Johnson et al., 2009; Castillo-Rogez et al., 2012) as its shape suggests an early relaxation to a nearly spherical object, possibly the result of internal heating. Nearly all of these objects have been imaged by Cassini at pixel scales of <300 m (Table S1), although not over their entire surfaces. These resolutions allow comparison of shapes, surface features, photometry, and colors. The basic shapes, densities, and some surface features of the small saturnian satellites have been discussed in Porco et al. (2005) (Phoebe), Porco et al. (2007) (ring satellites), and Thomas (2010). With the exception of Phoebe, all of these objects that have measured masses appear to have mean densities consistent with highly porous water ice. Other components are almost certainly present, but likely constitute onlysmall amounts (Filacchione et al., 2010; Buratti et al., 2010). Model porosities assuming a solid density of 930 kg m^{-3} (appropriate for water ice) are ~30–60%. Addition of a denser component would increase these model porosities.

This paper uses Cassini Imaging Science Subsystem (ISS; Porco et al., 2004) data obtained through mid-2012 to update the shapes and characteristics of these small satellites. Notably better data will not be obtained until 2015. We deal with all the inner groupings of the small saturnian satellites, but concentrate on the ring-arc embedded satellites and on the Trojan satellites co-orbiting with Tethys and Dione.

2. Data and methods

All images used are from the Cassini Imaging Science Subsystem (Owen, 2003; Porco et al., 2004); most are from the Narrow Angle Camera (NAC) which has a pixel scale of 6 km at a million km range. Shape models of the satellites have been gradually improved

* Corresponding author.
E-mail address: pct2@cornell.edu (P.C. Thomas).

0019-1035/$ - see front matter © 2013 Elsevier Inc. All rights reserved.
http://dx.doi.org/10.1016/j.icarus.2013.07.022

with data from multiple flybys at a variety of resolutions, viewing angles, and phase angles. The orbit of the Cassini spacecraft has changed during the mission to support different goals, some of which require high inclinations that lead to periods of months or years between close imaging of small satellites.

Stereo control point solutions are the basis of the shape models and libration studies. Control points are marked manually on images covering as wide a range of observer geometries as possible with the POINTS program (J. Joseph; in Thomas et al. (2002)Thomas et al. (2002)). Some additional control points have been added through automated image matching, but these are a small minority of the points that are used. Resolutions of the images used vary greatly due to the nature of the different flyby trajectories. Residuals of the control point solutions (predicted vs. observed image locations) are typically 0.3–0.4 pixels. Shape models are fit to the stereo points, and modified based on limb profiles. The shape models are derived in the form of latitude, longitude, radius at 2° intervals in latitude and longitude (Simonelli et al., 1993) but for some purposes can be converted to more evenly spaced x, y, z triangular plate models. In some cases Saturn-shine or silhouettes of the satellites in front of Saturn provide crucial coverage of limbs or of control points. Description of the techniques are in Simonelli et al. (1993) and Thomas et al. (2007a).

Solving for the control points requires knowledge of the instantaneous orientation of the object. Correctly predicting the satellites' orientations requires accurate orbital and rotational data, including information on any forced libration (Tiscareno et al., 2009). Our model for Helene's orientation is of the same form as that described by Tiscareno et al., based on the moon maintaining synchronous rotation (even as the orbit frequency changes due to the co-orbital resonance) with additional librations of variable amplitude that track the instantaneous orbit frequency. More detailed dynamical analysis (Noyelles, 2010; Robutel et al., 2011a) confirmed in the case of Janus and Epimetheus that there are no observable deviations from the Tiscareno et al. model, as expected for a moon whose rotational dynamics are dominated by in-plane forced librations due to its non-spherical shape. Although Robutel et al. (2011b) recently presented a detailed dynamical analysis of the orientation of Helene, we choose for this work to continue using the Tiscareno et al. model, which gives sufficient precision, is easy to implement, and is physically intuitive. The control-point solutions for Helene suggest any forced libration is <1° (Fig. S3). Predictions on possible forced librations based on the shape model alone are limited both by necessary assumptions of a homogeneous interior as well as low-resolution views of some longitudes, and the presence of an as-yet unimaged region including the north pole. The model moment ratio from the current shape model for $(B-A)/C$ is 0.014, which would predict physical librations of <0.1°, a value we are far from being able to detect.

For Calypso and Telesto, we obtained sufficiently precise control point results from a model assuming a constant rotation rate, as any librations were undetectable probably due to their smaller amplitudes of libration in the co-orbital resonance (Oberti and Vienne, 2003; Murray et al., 2005).

For the more ellipsoidal objects, shapes are determined by measurement of limb coordinates for an analytical ellipsoidal fit. Scans are taken in images along line or sample directions and the position of a sharp bright edge is modeled in steps of 0.05 pixels; the limb coordinate is selected as the best match of predicted and observed brightness. The line and sample coordinates so obtained are corrected for spacecraft range and optical distortion to relative positions in km in the viewing plane. An ellipsoid is then fit to views from different directions, allowing the three ellipsoidal axes and the coordinate center to vary. The uncertainties in range and orientation of the image are assumed to induce errors in the shape that are small compared to other sources of error; see Dermott and Thomas (1988) for a discussion of the effects of such errors on the solutions. Precision of the limb measurement is commonly better than 0.1 pixel. The uncertainty in ellipsoidal solutions depends on the limb topography (roughness, or how close to an ellipsoid it is), resolution, and the spread of viewpoints that constrain the solution.

Crater counting and feature mapping are done interactively with the POINTS program. Features are mapped using manually stretched images. Locations of mapped points are the projection of single points, or centers of ellipses (such as crater rims) on the shape model in particular images. Data are stored in text files that include body-centered and image locations, and image and lighting information. Past experience in mapping irregular objects shows that crater counts are reliable down to diameters of 5–7 pixels and in images above 45° phase. Mapping coordinates use West longitudes, per the IAU rules for satellites (Archinal et al., 2011), and 0°W is on the (on average) sub-Saturn point. Topography is described by dynamic heights (H_d; Vanicek and Krakiwsky, 1986; Thomas, 1993) which are similar to, but not identical with, heights above an equipotential. H_d is the potential energy at a point on the surface divided by an average surface acceleration. The potential energy calculation accounts for the irregular shape of the body's mass assuming uniform density, and rotational and tidal accelerations.

For our photometric work we first radiometrically calibrated the ISS images with the CISSCAL computer program, which is available through the Planetary Data System (PDS). Details of the ISS Camera calibration are given in West et al. (2010), Porco et al. (2004), and the CISSCAL User's Manual (http://pds-rings.seti.org/cassini/iss/software.html). In the calibrated images, pixel DN values are scaled to radiance factors, $I/\not{F}$, where I is the specific scattered intensity of light and $\pi\not{F}$ is the specific plane-parallel solar flux over the wavelength range of the filter bandpass. We rely on the four ISS NAC multispectral filters that were most frequently used during close-flybys as well as distant imaging of the satellites; CL1–CL2 (611 nm), CL1–UV3 (338 nm), CL1–GRN (568 nm), and CL1–IR3 (930 nm). Sampling of whole-disk and disk-resolved photometric measurements follows the approach of Helfenstein et al. (1994). In general, disk-resolved measurements were obtained only from images for which the diameter of the object in pixels was larger than 100 pixels. Local angles of incidence (i), emission (e), and phase angle (α) on the surfaces of the satellites were obtained using the appropriate satellite shape model and corrected camera pointing geometry via the POINTS program, cited earlier. From each image, the pixel-by-pixel disk-resolved radiance factors were measured and binned into 10° increments of photometric latitude and longitude.

3. Ring satellites

3.1. Pan, Atlas, Daphnis

These objects have been studied previously by Porco et al. (2007) and Charnoz et al. (2007). Pan (mean radius R_m, of 14 km) within the Encke gap of Saturn's A ring, and Atlas (R_m = 15 km), just outside the A ring, have been imaged at sufficient resolution to show distinct equatorial ridges giving these somewhat elongated objects "flying saucer"-like shapes. (Fig. 1, Table 1). Daphnis (R_m = 3.8 km) is also elongate and although it is less well-resolved than Pan and Atlas in terms of pixels/radius, it does have low-latitude ridge and is also somewhat saucer-shaped in that the a and b axes are both fractionally much larger than the c axis. These three objects rotate at least approximately synchronously with their orbital periods; synchroneity must be estimated by congruence of shape models at scattered, low-resolution views. Atlas is within

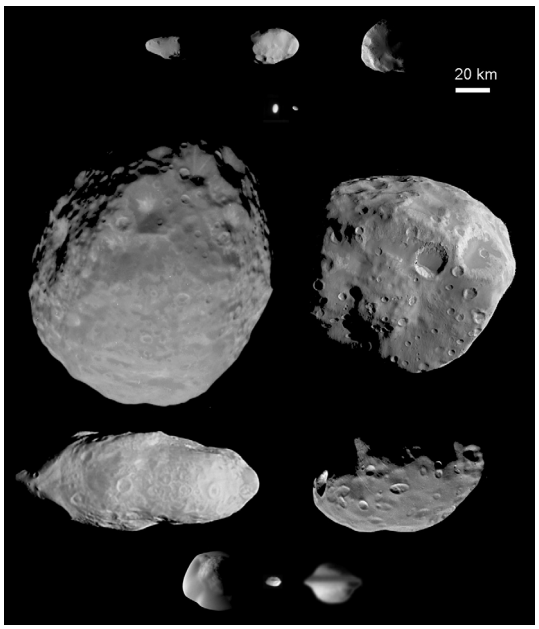

Fig. 1. Montage of primary study objects. Best images scaled to 250 m/pixel (see Table 1). Top row: Calypso: N1644754596; Telesto: N1507754947; Helene: N1687119756. Second row: Pallene N146910452; Methone N1716192103. Third row: Janus: N164934235; Epimetheus: N1575363139. Fourth row: Prometheus: N1640497752; Pandora: N1504613650. Bottom row: Atlas N1560303820; Daphnis N1656999330; Pan N1524966847. Note that the Pan image is partly obscured by ring material (just above the middle).

~15° of synchronous over 4 years; Pan ~20° over 4.5 years; Daphnis ~30° over 3.5 years. Geometrically all of these values could have multiples of 360° added. The elongate shapes and low mean densities (Table 1) indicate that the surfaces of these three moons have very low escape velocities, and crudely approximate shapes of Roche lobes (Porco et al., 2007). Consequently, additional accreted material would be only loosely bound. This property is also found on Mars' Phobos (Dobrovolskis and Burns, 1980) and Jupiter's Amalthea (Burns et al., 2004). Charnoz et al. (2007) note that the latitudinal extent of the equatorial ridge of Atlas is close to the range of vertical motion of the satellite relative to the ring. They model accretion of the equatorial ridges from ring particles. The considerable range of dynamic heights (H_d) on the surfaces of ring-related satellites is not reduced by modeling the presence of cores. Models of these objects with dense (900 kg m^{-3}) cores and very porous (150 kg m^{-3}) mantles cannot be discriminated from homogeneous interior models (Porco et al., 2007). (Here we use "core" to denote a denser central region, not implying any thermal differentiation process.) The models do show a large range of surface gravity (for homogeneous models; Table 1) that is typical of elongate, low-density, rapidly rotating objects. For these objects, all surface accelerations are still inward; that is, material is bound gravitationally to their surfaces.

Of these three objects, only Atlas has image coverage of sufficient resolution (250 m/pixel) to allow some discussion of surface morphology. The equatorial ridge is smoother than terrain at higher latitudes, but is not gravitationally flat: it has substantial slopes. For a homogeneous interior, relative dynamic heights along the equator vary by several km; the local acceleration and escape speeds (Fig. 2) also vary substantially around the equator. Both Atlas and Pan have relative gravitational topography that is large compared to their radii. The equatorial ridge on Atlas is gravitationally several km higher than the surface at mid-latitude regions, and is flanked by slopes relative to gravity of ~20°. This greater relative height of the equatorial region is different from that of some asteroids (Ostro et al., 2006; Harris et al., 2009) where equatorial ridges formed on rapidly spinning objects are gravitationally low and accumulate materials moving from gravitationally higher areas at greater latitudes. The large range of H_d on Atlas and Pan suggests that their shapes are not close to gravitational equilibrium conditions, no matter what the shaping mechanism, be it surface flow or accretion from outside. Extra accretion from ring-plane material may explain the ridges (Charnoz et al., 2007). If the ridges are composed of material less dense than a core, the relative gravitational height of the ridge crest would be greater than for the homogeneous model.

Topography on Atlas south of −30° has a lumpy appearance with some subtle, crudely east–west ridges ~2 km wide (N–S) and 3–5 km long (Fig. 2). It may have as many as five impact craters over 1 km in diameter in this area; these require viewing multiple stretches of the images and blinking images to see round forms that reproduce image-to-image (Fig. S1). Hirata and Miyamoto (2012) identified only one possible crater on Atlas, different from those mapped here. If these are indeed impact craters their muted topography suggests surface processes that erode and redistribute materials are nearly rapid enough to match crater formation rates. If they are not craters the conclusion is simply that recent rates of surface processes completely erase craters.

Table 1
Properties of irregularly-shaped saturnian satellites.

Satellite	A (km)	B (km)	C (km)	R_m (km)	Mass	ρ (kg m^{-3})	g (cms^{-2})	best (km/pixel)	Pixels/radius
Pan	17.2 ± 1.7	15.4 ± 1.2	10.4 ± 0.9	14.0 ± 1.2	0.495±.075	430 ± 150	0.01–0.18	1.2	12
Daphnis	4.6 ± 0.7	4.5 ± 0.9	2.8 ± 0.8	3.8 ± 0.8	.0077±.0015	340 ± 260	0.01–0.04	0.45	8
Atlas	20.5 ± 0.9	17.8 ± 0.7	9.4 ± 0.8	15.1 ± 0.8	0.66 ± 0.045	460 ± 77	0.02–0.19	0.25	60
Prometheus	68.2 ± 0.8	41.6 ± 1.8	28.2 ± 0.8	43.1 ± 1.2	15.95 ± 0.15	470 ± 44	0.13–0.58	0.20	217
Pandora	52.2 ± 1.8	40.8 ± 2.0	31.5 ± 0.9	40.6 ± 1.5	13.71 ± 0.19	490 ± 60	0.26–0.60	0.31	131
Epimetheus	64.9 ± 1.3	57.3 ± 2.5	53.0 ± 0.5	58.2 ± 1.2	52.66 ± 0.06	640 ± 62	0.64–1.1	0.22	323
Janus	101.7 ± 1.6	93.0 ± 0.7	76.3 ± 0.4	89.2 ± 0.8	189.75±.0006	630 ± 30	1.1–1.7	0.18	496
Aegaeon	0.7 ± 0.05	0.25 ± 0.06	0.2 ± 0.08	0.33 ± 0.06				0.10	3
Methone	1.94 ± 0.02	1.29 ± 0.04	1.21 ± 0.02	1.45 ± 0.03				0.03	54
Anthe				0.5				5.3	<1
Pallene	2.88 ± 0.07	2.08 ± 0.07	1.8 ± 0.07	2.23 ± 0.07				0.16	14
Telesto	16.3 ± 0.5	11.8 ± 0.3	9.8 ± 0.3	12.4 ± 0.4		–		0.059	210
Calypso	15.3 ± 0.3	9.3 ± 2.2	6.3 ± 0.6	9.6 ± 0.6		–		0.13	74
Polydeuces	1.5 ± 0.6	1.2 ± 0.4	1.0 ± 0.2	1.3 ± 0.4				0.41	7
Helene	22.5 ± 0.5	19.6 ± 0.3	13.3 ± 0.2	18.0 ± 0.4				0.042	424
Hyperion	180.1 ± 2.0	133.0 ± 4.5	102.7 ± 4.5	135 ± 4	561.99 ± 5	544 ± 50	1.7–2.1	0.014	9640
Phoebe	109.4 ± 1.4	108.5 ± 0.6	101.8 ± 0.3	106.5 ± 0.7	829.2 ± 1	1638 ± 33	3.8–5.0	0.013	8190

Masses for Janus, Epimetheus, Atlas, Prometheus, and Pandora are from Jacobson et al. (2008). Masses for Pan and Daphnis are from Porco et al. (2007). Mass of Hyperion from Thomas et al., 2007b. Mass of Phoebe is from Jacobson et al. (2006). Masses are in units of 10^{19} g.

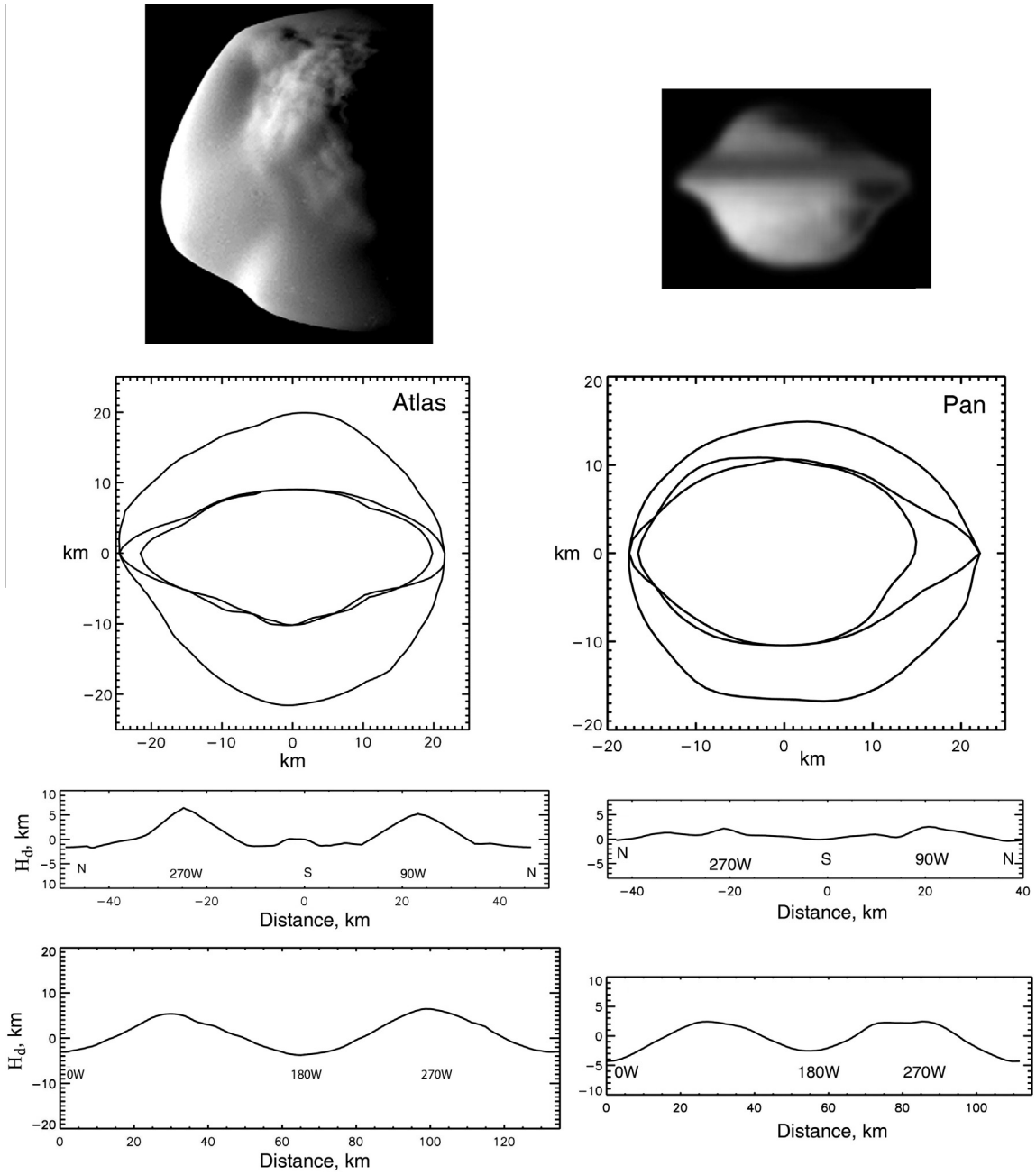

Fig. 2. Cross sections and gravitational topography (dynamic heights, H_d) of Atlas and Pan. Top: images from Fig. 1 of Atlas and Pan. Second row: cross sections, viewing equator profile (largest), and 90–270°W longitude profiles (smaller of inner sections), and 0–180°W longitude profiles (more elongate of inner profiles). Third row: H_d along 90–270°W longitude lines. Bottom row: profiles along equators. Note that vertical exaggerations vary in H_d plots.

Pan's equatorial ridge is relatively smaller than is Atlas' (Fig. 2). Image resolution of Pan is not sufficient to detect any textural contrasts between the equatorial region and higher latitudes. Daphnis is only a few pixels across in the image data, it is elongated, but no surface features can be resolved.

3.2. Prometheus and Pandora

Prometheus and Pandora shepherd the F ring, and having mean radii of 43 and 41 km, respectively, are far larger than Atlas and Pan. The mean densities of the F-ring shepherds are constrained to be slightly below 500 kg m^{-3} for both objects (Table 1). These elongate objects have substantial crater densities (see Section 6.5) and are more irregular and varied in form than are Pan and Atlas (Figs. 1 and 3). Pandora is a typical cratered, elongate, small object with some morphologic distinctions. First, it has grooves up to ~30 km in length in the trailing part of the northern hemisphere, most in a pattern of roughly parallel members oriented ~30° to the intermediate axis (Morrison et al., 2009). Second, it has several very shallow craters, some probably partly filled by ejecta. Other craters are shallow, elongate, and relatively young, similar in appearance to those common on Hyperion (Thomas et al., 2007a,b; Howard et al., 2012) (Fig. 1).

Prometheus is a heavily cratered object; much of its surface appears similar to those of Janus and Epimetheus. However, it is distinguished by global topography that suggests division into two terrains, one lower than the other and possibly representing an exposed inner core region. These terrains are bounded by long scarps (Fig. 3), features not seen on other small satellites. The only possible analogy on another small satellite might be the boundaries

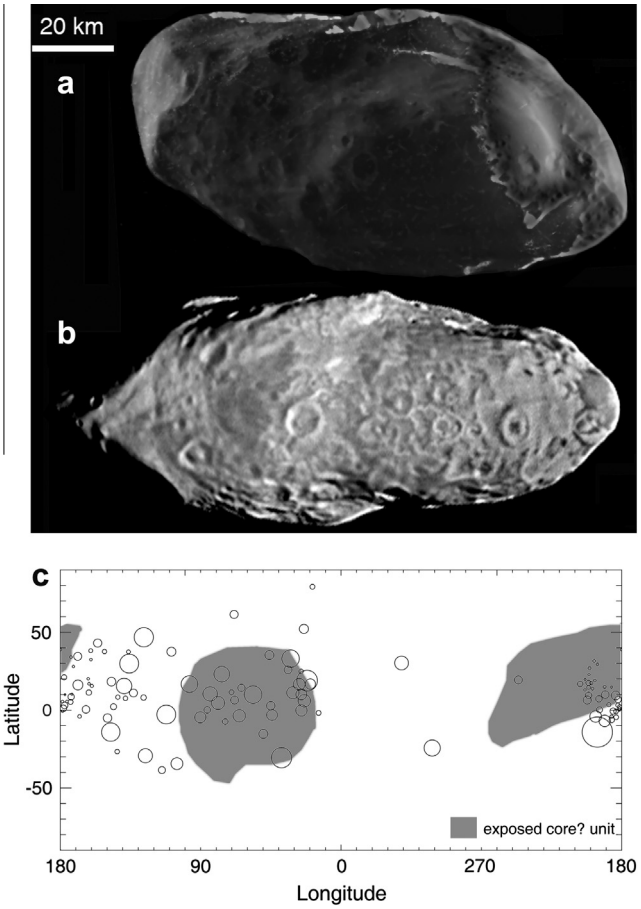

Fig. 3. Prometheus, showing possible expression of core. (A) Image N1643261394, from 19°N, 238°W, north is approximately up. (B) Image N1640497752 from 1°N, 100°W, north is approximately up. Image processing includes some high-pass filtering. (C) Map of exposure of distinct, lower terrain, possibly an exposed inner core or other distinct material. Major craters schematically mapped.

between the smooth equatorial regions of Atlas and the rougher, higher latitudes (Section 3.1). The lower terrain on Prometheus is densely cratered (Fig. 3); thus, if Prometheus is a partially delaminated object, that event happened at a large cratering age. We have approximated the shape of the region that might be an exposed core by interactively trimming the overall shape model to include smooth extensions of the lower terrain. The lower surface is exposed chiefly between longitudes 20–100°W and 170–260°W (Fig. 3c). The estimated volume of the putative core is 2×10^5 km^3, about 2/3 the whole object's volume of 3.4×10^5 km^3. The putative core is roughly an ellipsoid of semi-axes 60.5, 34.7, and 25.5 km.

4. Co-Orbitals Janus and Epimetheus

Janus (R_m = 89 km) and Epimetheus (R_m = 58 km) make up nearly 90% of the mass of the inner small satellites of Saturn (Table 1). They exchange orbits every 4 years (Dermott and Murray, 1981a,b; Yoder et al., 1989) and Epimetheus has been shown to have a forced libration of ~6° (Tiscareno et al., 2009). Early shape modeling work for Janus had suggested an offset of the minimum moment of inertia from Saturn-facing direction (Tiscareno et al.); however, the updated shape reported here has a moment offset of less than 1°, indicating there is no need to invoke substantial internal inhomogeneities. The mean densities of these two satellites are indistinguishable (640 ± 60 and 630 ± 30 kg m^{-3}) and are higher than those of the smaller satellites for which density data have been obtained (possible exception in upper limits of Aegaeon; see Section 5). These two moons are marginally more dense than Hyperion (544 ± 50 kg m^{-3}). The surfaces are heavily cratered (Section 7); both objects show a variety of crater degradation states as well as some ponding of materials in crater floors (Morrison et al., 2009; see especially Epimetheus in Fig. 1).

Epimetheus has grooves 5–20 km in length averaging ~1 km in width that are visible in the highest resolution images of the south polar region (Morrison et al., 2009). Some of these grooves display straight-walled morphology suggestive of graben, and thus indicate near-surface faulting. Most of these grooves trend parallel to the intermediate axis of Epimetheus, similar to some of the prominent grooves on Phobos' northern hemisphere and are distinctly different from the scattered patterns of grooves on asteroids Eros and Gaspra. At least one of the graben-like grooves cuts the rim of a 5-km crater.

5. Embedded satellites: Aegaeon, Pallene, Methone

Four small satellites lie beyond the orbits of Janus and Epimetheus: Aegaeon interior to Mimas and within the G ring; and Methone, Anthe, and Pallene orbiting between Mimas and Enceladus. These latter three satellites all have associated rings or ring arcs (Hedman et al., 2009). Anthe is only ~0.5 km in radius, and is not spatially resolved. Aegaeon (R_m = 0.3 km) is resolved a few pixels in width. Pallene (R_m = 2.2 km) and Methone (R_m = 1.5 km) have sufficiently good imaging data (Fig. 4) for accurate size measurements and that show them to be morphologically distinct from other small saturnian moons, and from any previously imaged small satellite, small asteroid, or comet nucleus.

5.1. Shapes

Results of shape fitting are given in Table 2. Aegaeon was seen in only one flyby in images of 91–127 m/pixel spanning ~22° in viewing angles. The images of Aegaeon (Fig. S2) are too small for our standard limb-finding software (the few pixels on the body substantially change brightness approaching the limb). The shape was obtained by matching expanded images of four views (Table S1) with ellipsoidal shape models changing in 50-m steps. Additionally, the high latitude of the viewpoints means the *c* axis is poorly constrained (largely by the terminator). We estimate the uncertainty in the fit axes at 0.08, 0.09, and 0.1 km for the *a*, *b*, and *c* axes, respectively. These uncertainties are large fractions of one pixel.

The disks of Pallene and Methone are large enough (Fig. 4) that the standard limb-fitting and error estimation are feasible. The allowable range of fit ellipsoidal axes is obtained by allowing the residuals (rms) to increase by 0.12 pixels (accuracy of this software determined from measurements of objects with independent, high-resolution shapes) above the minimum value. This evaluation gives uncertainties of 0.07 km for all Pallene axes. Methone's shape has calculated uncertainties (considered one sigma) of 0.02, 0.04, and 0.02 km for the *a*, *b*, and *c* axes, respectively. Note that although the views of Methone (Table 1) are only slightly better of the *a* axis (best view would be 90° from an axis) than of the *b* axis, the shorter *b* axis means that it affects projected ellipses less than does the *a* axis, hence the much greater calculated uncertainty in the *b* axis of Methone.

5.2. Inferred mean densities

We test whether the ellipsoidal shapes of these objects are consistent with effectively fluid, equilibrium shapes. Below in Section 5.5 we examine the more general problem of interpreting

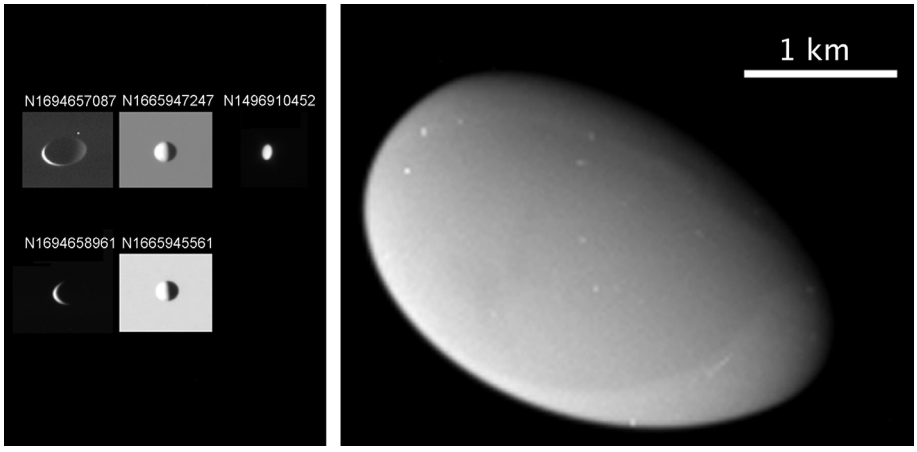

Fig. 4. Views of Pallene and Methone. Pallene shown in left set of five panels; km scales vary. Upper left image includes Saturn shine. Images with bright background are transit views. Right side, Methone image N1716192103, phase angle 63°. Spots are not reproduced image to image.

Table 2
Characteristics of embedded moons Aegaeon, Methone, and Pallene.

	Dimensions (km)							
	a	b	c	R_m	±			F
Ellipsoidal fits of shapes of embedded moons								
Aegaeon	0.70	0.25	0.20	0.33	0.05	0.06	0.08	0.10
Methone	1.94	1.29	1.21	1.45	0.02	0.04	0.02	0.11
Pallene	2.88	2.08	1.84	2.23	0.07	0.07	0.07	0.23

	Density (kg m^{-3})	min ΔH_d (km)	limit ΔH_d (km)	ρ_{min} (kg m^{-3})	ρ_{max} (kg m^{-3})
Inferred mean densities of embedded moons					
Aegaeon	540	0.035	0.070	410 (418)	700 (695)
Methone	310	0.008	0.020	280 (288)	330 (324)
Pallene	250	0.071	0.142	190 (194)	340 (338)

	Density (kg m^{-3})	g (cm s^{-2})	Escape (cm s^{-2})
Gravity of embedded moons			
Aegeon	540	0.0093–0.0127	2–17
Methone	310	0.0081–0.0130	19–87
Pallene	250	0.0106–0.0162	27–107

shapes of small, ellipsoidal satellites and asteroids, and explain why fluid-like behavior on geological time scales is an appropriate approach for these objects. If they have behaved geologically as fluids, inferences of mean densities may be made. Fluid-like behavior on geological times for these objects could involve any processes that disperse or transport material at the surface, and need only operate over depths of major craters on the body.

Fluid equilibrium shapes (unless otherwise stated, "equilibrium shape" is used as a fluid equilibrium; possible non-fluid equilibrium shapes are discussed in Section 5.5) of rapid rotators and low density objects are more prolate than the classical approximation with the shape parameter $F = (b-c)/(a-c) = 0.25$ (Chandrasekhar, 1969; Dermott, 1979). Mimas, a slightly faster rotator than the arc-embedded moons, with a density of 1150 kgm^{-3} has an equilibrium F of 0.21 (Thomas et al., 2007a,b). Because the exact equilibrium shape depends upon the mean density we test how much the observed shapes deviate from an equipotential surface as a function of assumed mean density. Using ellipsoid models of 3° resolution, we assume homogeneous interiors of varying density, and calculate the potential energy over the surface accounting for the distributed mass, rotation, and tidal effects (Thomas, 1993). If a particular mean density yields a very small range of dynamic heights (ΔH_d), the object may be acting as a relaxed fluid.

Table 2 gives the mean densities inferred from the minimum ΔH_d. Uncertainties in the inferred density may be calculated in multiple ways. One method is to do the ΔH_d calculation by allowing the shape models to change within observational errors and finding the range of densities covered by changing minima in ΔH_d. This approach gives density uncertainties of 50, 20 and 10 kg m^{-3} for Aegeon, Pallene, and Methone, respectively. We consider these values too optimistic, as they are substantially smaller than the physical measurement uncertainty. Our adopted approach uses the range of uncertainty in ΔH_d values induced by the range of possible shapes, and the consideration that the ideal situation would have a ΔH_d of 0 at the appropriate mean density. Because Methone has a best fit ΔH_d of only 8 m, for this object we test the range of H_d induced by the allowable range of the shape. The allowable range of shape for Methone (Table 2) produces a maximum range of H_d of 18 m, which we round up to 20 m ΔH_d as the allowable value for Methone. Mean densities that yield 20 m or less ΔH_d for the nominal shape of Methone are 288–324 kg m^{-3}, which we round to the wider range values of 280–330 kg m^{-3}. Pallene and Aegeon are less well measured, and we thus simply allow the range of ΔH_d to double from its minimum. The resulting inferred mean densities are given in Table 2, and the plots of H_d as a function of model mean density are shown in Fig. 5. We consider the Table 2 values to be reasonable estimates of 1-sigma uncertainties in the mean

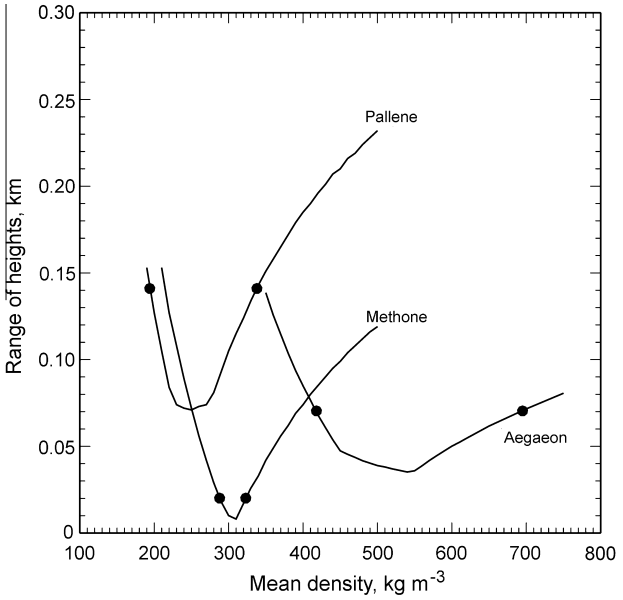

Fig. 5. Range of calculated dynamic heights for Aegaeon, Methone and Pallene as a function of mean density. Dots show inferred limits of acceptable solutions (see text). The somewhat segmented shapes of the curves reflect the changing loci on the surface of the minimum H_d which affects the incremental change in average gravity and hence the calculated ΔH_d range.

densities if the bodies are homogeneous and if they act as fluids over geological timescales, and if the shapes were set at the current orbital distances from Saturn.

We list in Table 2 the gravitational accelerations at the surface of the satellites and approximate ranges of escape velocities. The range of net surface accelerations arises from variations in radii and in rotational and tidal accelerations across the objects. "Escape" velocities have been calculated by tracking test particles (methods given in Thomas (1998)) launched radially from points across the surface, in velocity magnitude increments, and setting escape velocity for a particular site when the particle either stays aloft more than ½ orbital period or reaches 10 mean radii distance. Of course particles barely escaping will reimpact at some point, but this is a convenient measure for when material achieves a different "sedimentary" regime. Velocity vectors with different orientations would expand the range of calculated "escape" speeds as well.

5.3. Possible non-homogeneous interiors

Perfectly homogeneous interiors of these small satellites might be considered unlikely given some views of small objects, such as Asteroid 25143 Itokawa (Fujiwara et al., 2006), Atlas (Porco et al., 2007; Charnoz et al., 2007), and the expectation of either impact fracturing, or accretion of particles of various sizes and mean density that likely follow from differences in collisional history (Porco et al., 2007). The possible presence of denser cores that have acted as "seeds" for later accumulation invite tests of what the observed shapes would imply for equilibrium properties. We first note that a particular ellipsoidal equilibrium form has a lower mean density if centrally condensed than if it is homogeneous (Dermott, 1979). Thus, if the interpretation of a relaxed fluid state is correct, Methone must have some material of density less than 330 kg m^{-3} even if it has relatively denser material at depth. Likewise, Pallene and Aegaeon would have material equal to, or less than, their calculated maximum mean densities. Secondly, we note that any denser interiors are unlikely to be simple shapes, and thirdly, models are not unique but do show trends and limits.

The shape of Methone is the most accurately known of the arc-embedded objects, and thus we use it as an example of the kinds of mass distributions possible in these objects if they have denser cores. To test how the current shape of Methone may relate to a centrally condensed body, we assume a spherical core of density 660 kg m^{-3}: this density is twice the inferred upper homogeneous density limit of Methone and is similar to the bulk density of Janus and Epimetheus (Table 1). Computationally, the potential from a centered sphere of a particular size and density equal to (660 – 310) kg m^{-3} is added to the homogeneous solution and the same potential energy calculations are made for points on the surface. We initially use the nominal shape (semi-axes of 1.94, 1.29, 1.21 km) varying the core size, and find the mantle density that gives the smallest ΔH_d. These results, and the properties of the resulting models, are shown in Fig. 6. Very small cores are not detectable. Allowable solutions with ΔH_d of 20 m or less apply to core radii of 0.65 km with a core mass fraction of 0.25, and mantle density of 200 kg m^{-3}. Thus our solution of Methone allows for, and cannot distinguish among, core mass fractions of less than ~0.25. Small cores with density of >660 kg m^{-3}, or larger cores with lower mean densities, allow a range of surface material densities of ~200–330 kg m^{-3} for this object. A very large core with

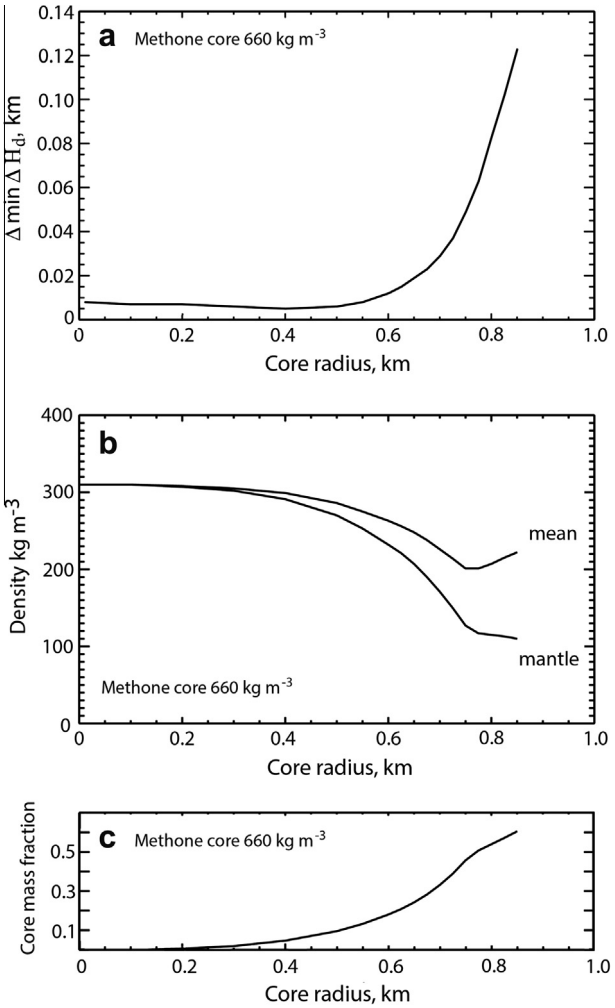

Fig. 6. Possible core configurations and properties of Methone with its nominal shape. (a) Minimum range of H_d over the surface as function of spherical core size. (b) Mean density and mantle density needed to produce the minimum ΔH_d for each core size model. (C) Core mass fraction for each core size.

only a very thin covering would necessarily have a mean density little different from the homogeneous case even if the thin surface layer has properties different from the mean.

5.4. The surfaces of Aegaeon, Pallene, and Methone: topography

Is the smooth surface of Methone (and Pallene and Aegaeon) unusual for small bodies? If so, what does that characteristic imply? The limb residuals are plotted for Pallene and Methone in Fig. 7; comparison plots for other small objects with similar resolution data are shown in Fig. 8. Methone clearly occupies a different roughness regime from the comparison objects. Another simple method of comparison is to calculate the supported topography in terms of ρgh (density $*$ gravity $*$ height). We use the maximum gravity calculated for each body. The density we take is the body's mean density, realizing that surficial materials may differ. For the height to consider for objects with known mean densities and good shape models, we calculate the range of H_d over areas of radius $0.1R_m$. For the small "egg" satellites, we simply use the minimum ΔH_d calculated for the whole object (these are roughly consistent with the deviations of limb topography). The tabulation of these admittedly rough measures are in Table 3. The egg satellites and comet nuclei have the lowest supported loads; satellites such as Atlas and Telesto support ~700 times the loads calculated for Methone. The loads as a function of object mean radius are plotted in Fig. 9. Objects other than Pallene and Methone and the three comet nuclei give a linear slope of 1.8, close to that expected from simply scaling shapes up (slope of 2) as g and h would both scale linearly with radius. The arc satellites and comets lie below the extrapolation from the other bodies.

Interior pressures on these objects are low; central pressure in a homogeneous Methone of mean density 310 kg m^{-3} would be ~30 Pa. The ~100 fold difference in the product of surface gravity and mean density between Janus and Methone means that pressures deep within Methone, a few hundred m, are equivalent to those at a few m depth on Janus, or a few cm depth on the Earth's Moon. The ability of these objects to sustain high porosity is not surprising.

The smoothness of Methone compared to other saturnian objects is shown in Fig. 10. The surfaces are compared at 42 m/pixel as the best pixel scales on any small satellite except Methone (27 m/pixel). In these images, at roughly comparable phase angles, it is clear that Methone is distinct. The other objects, except the sample of Helene, have variations on crater topography, which is

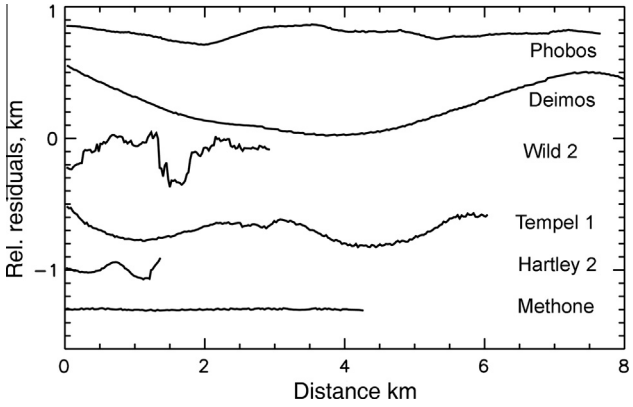

Fig. 8. Limb profiles from small objects. Vertical exaggeration = 2. These are radial residuals of limb profiles fit by ellipses; these are not gravitational topography. Data: Phobos, Viking image 854a62, 24.0 m/pxl, $\alpha = 45.2°$; Deimos Viking image 507a01, 32 m/pxl, $\alpha = 32.4°$; Wild 2 2079we02, 24.2 m/pxl, $\alpha = 72.2°$; Tempel 1 mv0173728278, 28.5 m/pxl, $\alpha = 63.4°$; Hartley 2 mv0342149134, 22.0 m/pxl, $\alpha = 83.1°$; Methone N1716192103, 27 m/pxl; $\alpha = 63°$.

lacking on Methone. The regions selected for Fig. 10 on the larger objects were specifically picked to try and avoid local effects of ejecta or tectonics (selected areas are small: 13 km on a side), a selection that required careful searching as ejecta from large craters and tectonic features are common. Atlas (Figs. 1 and 2) also appears smooth, but this is at ~10 times worse resolution than the best Methone images, and it does show at least two possible crater outlines in the low-latitude, smoother regions. While there may be smoothing of topography at fine scales on Atlas, the process(es) involved have not reduced regional slopes: in the low latitude regions they are 10–30° (see Fig. 2).

The supported load values quantitatively emphasize the visual impressions: the arc/ring embedded moons are unique among small Solar System bodies so far imaged. All other bodies $\lesssim$200 km mean radius that are equally well imaged (and many that are much more poorly imaged) show effects of cratering or other variegations in form that distinguish them from ellipsoids. What is unique about these moons? The most obvious distinguishing factor is their presence within rings/arcs, and it is this association we first explore.

The moons' presence in ring arcs suggests cycling of material between satellite and ring-arc might contribute to a unique appearance. Because there are no visible craters over ~130 m

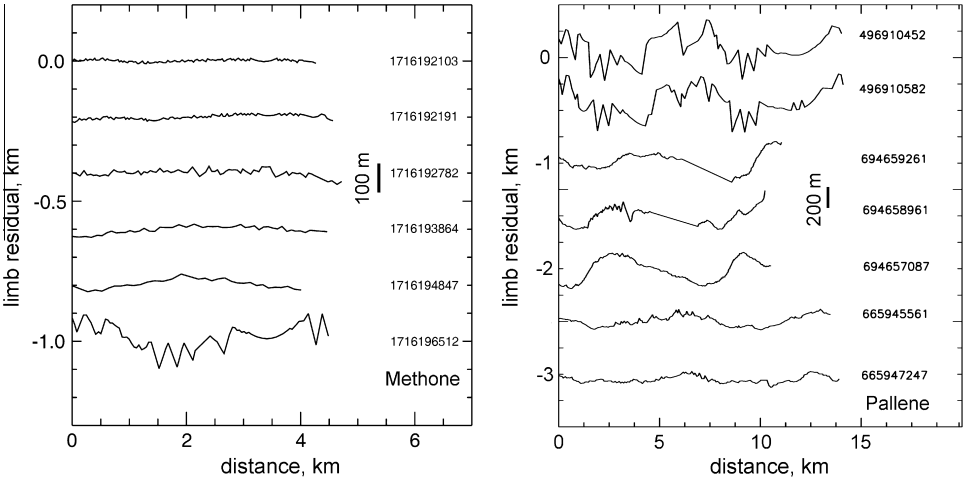

Fig. 7. Limb residuals for Methone (left) and Pallene (right). Note different scales for Methone and Pallene plots. Top Methone image is 27 m/pixel, bottom Methone image is 161 m/pixel. Top: Pallene image is 460 m/pixel, bottom is 220 m/pixel.

Table 3
Supported stresses on small objects.

Object	g (cms^{-2})	h (m)	ρ (kg m^{-3})	ρgh (Pa)	R_m (km)
Hartley 2	0.0037	17.	300	0.19E+00	0.5
Methone	0.013	08.	310	0.32E+00	1.4
Itokawa	0.01	10.	1900	0.19E+01	0.26
Wild 2	0.02	30.	400	0.24E+01	2.0
Pallene	0.016	71.	250	0.28E+01	2.2
Tempel 1	0.038	60.	400	0.91E+01	2.8
Calypso	0.14	170.	500	0.12E+03	9.5
Deimos	0.27	35.	1440	0.14E+03	6.2
Atlas	0.19	250.	460	0.22E+03	15.1
Telesto	0.18	280.	500	0.26E+03	12.4
Steins	0.13	200.	2000	0.52E+03	2.2
Helene	0.39	440.	400	0.69E+03	18.0
Phobos	0.63	155.	1870	0.19E+04	11.1
Pandora	0.60	790.	490	0.23E+04	13.7
Eros	0.56	184.	2600	0.27E+04	8.4
Prometheus	0.58	1510.	480	0.42E+04	15.9
Epimetheus	1.10	1300.	340	0.49E+04	52.7
Ida	1.03	370.	2640	0.10E+05	15.7
Mathilda	0.93	780.	1300	0.94E+04	26.5
Janus	1.69	1560.	640	0.17E+05	89.0
Hyperion	2.10	2980.	540	0.34E+05	135.0
Miranda	7.90	1400.	1200	0.13E+06	235.8
Phoebe	5.00	2770.	1640	0.23E+06	106.5
Vesta	22.00	5000.	3400	0.37E+07	265.0

Densities of Wild 2, Steins, Calypso, Telesto, and Helene are assumed. Other properties from Fujiwara et al. (2006), Brownlee et al. (2004), Russell et al. (2012), Thomas (1993), and Keller et al. (2010).

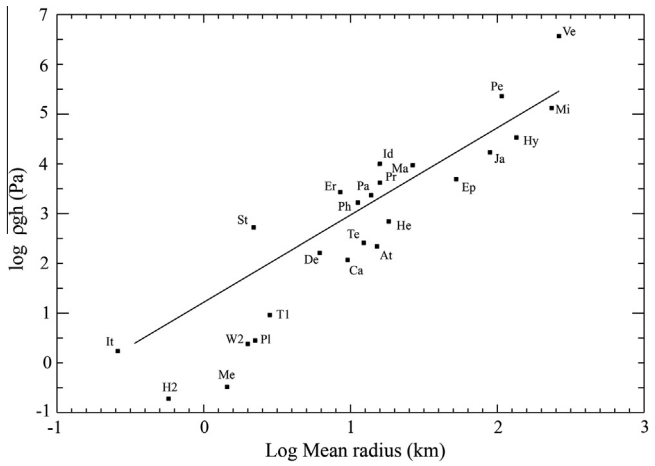

Fig. 9. Supported loads on small objects; see text and Table 3. It: Itokawa; H2: Hartley 2; Me: Methone; W2: Wild 2; Pl: Pallene; St: Steins; T1: Tempel 1; De: Deimos; Er: Eros; Ca: Calypso; Ph: Phobos; Te: Telesto; Pa: Pandora; At: Atlas; Pr: Prometheus; Id: Ida; He: Helene; Ma: Mathilde; Ep: Epimetheus; Ja: Janus; Pe: Phoebe; Hy: Hyperion; Mi Miranda; Ve: Vesta. Straight line is linear log fit to objects other than comets and ring-embedded objects.

(5 pixel diameter) over ~9 km^2 of surface, surface processes are erasing craters having relief of many tens of m as fast as they are formed. The collision time of Methone (or any of the moons) with a grain that resides in – and moves back and forth within – the associated arc can be calculated by turning the measured optical depth into a number density (assuming a single size of particle). Knowing the relative speed between grains and Methone, which is roughly the typical random velocity, we could then calculate the time for Methone to run into essentially all the grains in the arc.

Alternatively, and more simply understood, we note that particles (and moons) in the resonant arcs have libration periods of a year or two. In one libration period, the moon will have swept the full length of the arc and hence would be coated with an optical depth (τ) of arc material. However, we need to keep in mind that the quoted optical depth is a normal optical depth whereas the moons move longitudinally along the arc. Thus the appropriate optical depth is the normal optical depth times the arc length divided by the arc's width or thickness, assumed to be the same.

For our cases, τ is ~10^{-7}. Typically the arc lengths are the circumference (~10^7 km) divided by the resonance number, ~10 (or we can use the observed length since the full resonance well is not populated usually); and the measured widths (proxy for thicknesses) are about 100 km. So this raises the optical depth seen along the arc to 10^{-3}. Hence coating times are about 10^3 yrs, but this is just the period needed to be coated by 1-μm grains.

To get more realistic resurfacing times, we can look at the masses in the two arcs that have absorbed magnetospheric electrons: the G ring arc (see Hedman et al., 2007) and Methone's arc (see Roussos et al., 2008). The former argues that unseen large particles (needed to absorb the energetic electron population) account for 10^3–10^5 times as much mass as is visible in the optical images. The latter comes to a similar conclusion, namely that the microsignature that was used to infer the arc's presence can either be a relatively high optical depth (10^{-3}) of 1 μm particles, or a lower optical depth (10^{-7}) of several mm particles; later observations showed the lower optical depth population to be present. In either case, most of the absorbing mass (which is what also matters for covering surface features) is in particles that cannot be detected optically.

Covering by microns in 10^3 yrs, or mm in 10^7 yrs implies rates of order 1 m/10^{10} yrs. Such rates would be overwhelmed by impact cratering gardening (Dones et al., 2009). The inferred surface environments of the arc-embedded objects, very low gravity and low density material, may also promote formation of much larger craters than on more "normal" objects. Predictions by Richardson and Melosh (2013) for the surface of Comet Tempel 1, somewhat similar in gravity and mean density to Methone, suggest an impact crater in loose material of strength ~1–10 Pa (~"mountain snow") would be an order of magnitude larger than one formed in material of strength ~1000 Pa ("soil"). The latter is much weaker than solid rock and perhaps much closer to materials on objects 10's to 100's of km in mean radius than to the material at the surface of Methone. Key to comparing hypothesized surface process rates to impact turnover rates is a better understanding of the present-day small-impactor environment near Saturn.

The low rates of resurfacing from ring/arc material reflect the small mass of material currently in the arc, perhaps enough for one layer of particles, and inform us that the arcs are most likely an effect of whatever surface processes are smoothing these satellites, rather than its cause. Our knowledge of likely processes on such low-gravity, low-density objects is minimal. Electrostatics have been suggested as facilitating small particle motions on a variety of objects including small saturnian moons (Hirata and Miyamoto, 2012), but modeling the real conditions, and the need for some topography and local contrasts in exposure to illumination and charged particles render the efficacy of this process highly uncertain. Flows on comet Tempel 1 (Veverka et al., 2013) and deposits on Hartley 2 show the possibility of movement of large volumes of porous materials is possible on small objects, but most likely these examples depend on volatile action, an unlikely process on objects at <100 K. One might speculate that hypervelocity impacts into particularly porous water ice might release local bursts of water vapor that might fluidize some regolith materials. Of course, this speculated occurrence might actually tend to weld particles instead of fluidize them. Harris et al. (2009) note that in binary asteroidal systems tidally-induced changes in surface gravity might lift and transport particles ("tidal saltation"). However,

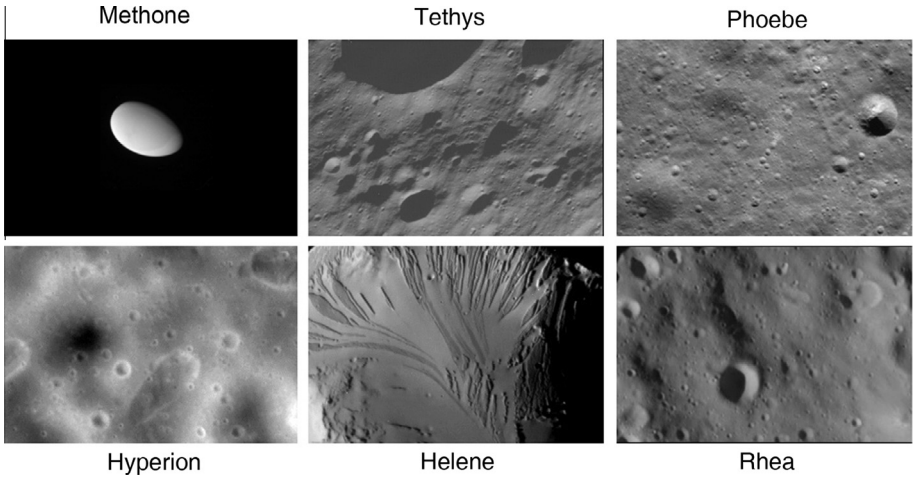

Fig. 10. Views of Saturn satellites at 42 m/pixel. Top row, from left: Methone, N1716192103; Tethys: N1506222566; Phoebe: N1465674412. Bottom row from left: Hyperion: N1506393440; Helene: N1687119756; Rhea: N1567129584. Each panel is 13 km wide.

the arc-embedded satellites do not have companions to raise tides, only the passing small components of the low-optical depth rings.

5.5. Geophysical interpretations of ellipsoidal-shaped satellites (and asteroids)

Newton's *Principia* noted that, when the Earth is considered to be a spinning homogeneous fluid, its density determines its ellipsoidal shape; of course, stars and gaseous planets behave similarly. Over geological timescales, some solid satellites and asteroids apparently flow to adopt fluid-like shapes whose precise forms depend upon central density concentrations (see Section 5.3). In contrast, small, cold outer-Solar-System bodies are unlikely to develop fluid-like shapes on any timescale. Our ever-expanding library of well-imaged, irregularly shaped small satellites, asteroids, and cometary nuclei reinforces the notion that fluid approximations are rarely useful for explaining the shapes of such objects (Thomas, 1989). Nonetheless, regions on a few such bodies are smooth, suggesting they might form equipotential levels when surficial materials are transported and deposited into "gravitational" lows. Everyday terrestrial experiences with soils, gravels, and grains clearly indicate that granular materials can flow under appropriate conditions but also can indefinitely support slopes whose steepness varies with friction angle. Accordingly, equilibrium (non-deforming) shapes for satellites and asteroids have been modeled (e.g., Holsapple, 2001, 2004; Richardson et al., 2005; Holsapple and Michel, 2008; Sharma et al., 2009; Sharma, 2009, 2013) according to their material properties and loading (e.g., rotational stresses, tides or YORP-induced spin-up.

We now evaluate the applicability and implications of the granular equilibrium shape models both theoretically and observationally. The theoretical basis of the granular equilibrium ellipsoids is the object's material responding to some failure criterion, such as the Mohr–Coulomb (Holsapple, 2004) or Drucker–Prager (Sharma et al., 2009) laws. In the simplest application, friction angles of the materials (Harris et al., 2009) limit equilibrium morphologies rather than the mean density as in the fluid equilibrium case, but a more complete theory (Sharma et al., 2009) provides similar results. Although computational methods vary, fundamentally the granular equilibrium models determine the shapes of objects under specified rotational and tidal conditions that do not exceed failure criteria set by angles of friction. Lower effective friction angles allow a smaller range of permitted equilibrium shapes for a particular orbital position and object density; the limiting case of a 0° friction angle produces fluid shapes. What happens in actual failure is not simply determined (Holsapple, 2001, 2004; Harris et al., 2009; Sharma, 2013).

It is doubtful whether these limiting ellipsoidal shapes could ever actually occur because the sequence of processes that would produce such morphologies without previous failure is unknown. Indeed, one should not expect that processes dependent on frictional failure could generate a smooth ellipsoidal object. In terrestrial examples, the collapse of granular structures leads to locally regular slopes, but these occur within variegated landforms as a whole because the granular sliding requires an additional landform as a source for the materials. Dune slip faces – the most regular of granular slopes – cannot exist without associated mounded, less-sloped landforms. Scree slopes need scarps or gullies. All sliding landforms also require a base or intersection with a differently sloped sliding surface. We also note an additional theoretical conundrum for granular ellipsoidal models: on ellipsoidal satellites in synchronous rotation, no matter what the symmetric mass distribution, slopes will be 0° at the principal axes, and will be greater elsewhere, except in a fluid case where they would be 0° throughout. Thus, theoretical limits on the dimensions of granular bodies do not mean that the formation of granular ellipsoids by sliding failure is possible.

In a few cases, nonetheless, an object's shape appears to be substantially modified by its granular nature: we refer to rapidly spinning asteroids where material evidently failed and shifted toward the equator reshaping the object (Ostro et al., 2006; Harris et al., 2009; Brozovic et al., 2010, 2011; Busch et al., 2011; Benner et al., 2012; Nolan et al., 2012). We emphasize, as noted by Harris et al. (2009) when discussing 1999 KW4, that these bodies are NOT ellipsoids, and that the failure occurs only across a restricted latitude range. The sharp angular boundary with the opposing hemisphere's slopes demonstrates the restriction of sliding-related shapes to non-ellipsoidal forms. Essentially all small Solar-System objects, except the saturnian arc-moons that we discuss here, show irregularities, such as craters, ridges, slumps, and grooves meaning that they are not smooth ellipsoids. Owing to the presence of steep crater slopes and other forms, all of these well-imaged objects suggest that at least large fractions of their volumes have friction angles expected of geological materials: 30–40° (Harris et al., 2009; Sullivan et al., 2011). In the instances of sliding on rapidly spinning objects the outcomes are as expected and are not ellipsoidal in shape.

What about fluid behavior? Because local, essentially flat surfaces (e.g., the ponded deposits on Eros as surveyed by Robinson et al., 2001) are known, conditions must occasionally occur on

small, airless objects wherein at least some regolith is fluidized. Asteroid Itokawa furnishes another example: smooth, low areas (slopes <1.2°; Barnouin-Jha et al., 2008) probably contain ~cm-scale particles that should be able to sustain substantial static slopes, but apparently have relaxed to an essentially level deposit. Distinctly filled craters are visible on Epimetheus (Fig. 1), suggesting the flow and segregation of a mobile regolith component that was emplaced just like a fluid. Similarly, material has drifted across Deimos' surface despite slopes of only ~2° (Thomas et al., 1996); this is geologically indistinguishable from fluid behavior. Yet the key distinguishing element for Saturn's arc-moons is the presence of consistent properties or regolith dynamics over the entire visible surface such that the object maintains a smooth ellipsoidal form. Comparable, global-scale features have not been observed on any other well-imaged small body. Landforms dominated by frictional properties are inherently variegated (note the example of 1999 KW4, Fig. 3 in Ostro et al. (2006)). Absent indications that whole objects can be modified to approach an ideal failure envelope, for interpretations of individual, specific smooth ellipsoids, it seems more fruitful presently to employ geophysical assumptions based on fluid-like geological behavior. Such fluid-like behavior need only extend to depths sufficient to flatten competing forms such as crater rims and bowls.

5.6. The surface of Methone: photometry

Methone's leading-hemisphere exhibits three conspicuous albedo features; a sharply-bounded, relatively dark oval centered on the leading hemisphere, an even darker irregular splotch that is centered almost exactly at the apex point on the body, and relatively bright material that surrounds the dark oval (Fig. 11a). For this photometric analysis we used the well-known Minnaert (1941) photometric model ($(I/F) = B_0 \cos^k(i)\cos^{k-1}(e)$ where B_0 and k are the two model parameters to correct for incidence and emission angles. Our best-fit Minnaert parameters for each image are given in Table S2; summary results are given in Table 4. To produce the albedo map, the photometrically corrected brightness values from each image were renormalized to represent normal albedos at ($i = 0°$, $e = 5°$, $\alpha = 5°$) prior to map projection. We applied least-squared fits to the CL1–CL2 filter results giving $B_0 = -0.00396\ \alpha + 0.6372$ and $k = -0.00309\ \alpha + 0.887$ for the phase dependence of the Minnaert parameters. To optimize the spatial details, areal coverage, and to reduce mapping artifacts, we combined map panels from the CL1–CL2 filter with the best-resolution images in the CL1–UV3, CL1–GRN, CL1–IR1, and CL1–IR3 filters. The brightness of the color-filter albedo images were adjusted to match those of the CL1–CL2 filter by applying the corresponding ratios from the Minnaert fits. An iterative approach was also applied to further adjust the contrast levels in the color filter panels so that they best-matched those in the overlapping regions in the CL1–CL2 filter panels. Following the approach summarized in Helfenstein et al. (1989), pixel-by-pixel weighted averaging was done to merge the individual map panels into the composite map.

Table 4
Normal albedos on methone.

Evaluated at $\alpha = 5$, $i = 0$	
Leading side	0.618 ± 0.086 (0.024)
Inner dark area	0.605 ± 0.040 (0.003)
Dark oval	0.614 ± 0.081 (0.025)
Bright surrounding	0.633 ± 0.086 (0.010)

Uncertainties listed include a contribution from extrapolating albedos to 5° phase angle and a ~5% absolute radiometric calibration uncertainty. Parentheses give 1σ relative errors.

Normal albedos for the visible features are given in Table 4. Within the expected uncertainties, the average normal albedo of the visible leading-hemisphere (0.62 ± 0.09) is broadly consistent with the geometric albedo of 0.57 ± 0.05 obtained from Methone's whole-disk phase curve (see below). IR3/UV3 ratios show no trend with albedo (Fig. 11b); the average IR3/UV3 ratio in all three albedo divisions is 1.26. The absence of correlated patterns of color and albedo on Methone suggests that the distinct albedo pattern is not the result of systematic variations in surface composition. Rather, the patterns may arise from variations in some other surface physical property, such as regolith grain size, soil compaction, or variations in particle microstructure. Neither the contrast amounts, nor the presence of a leading-side albedo marking are unusual for this marking. What is distinctive is the sharp boundary, the precise centering on the leading point, and the additional "swirl" feature at the leading point. It is not yet known whether similar patterns exist on the other arc-embedded satellites or the extent to which the pattern might exist but be obscured by surface relief on more

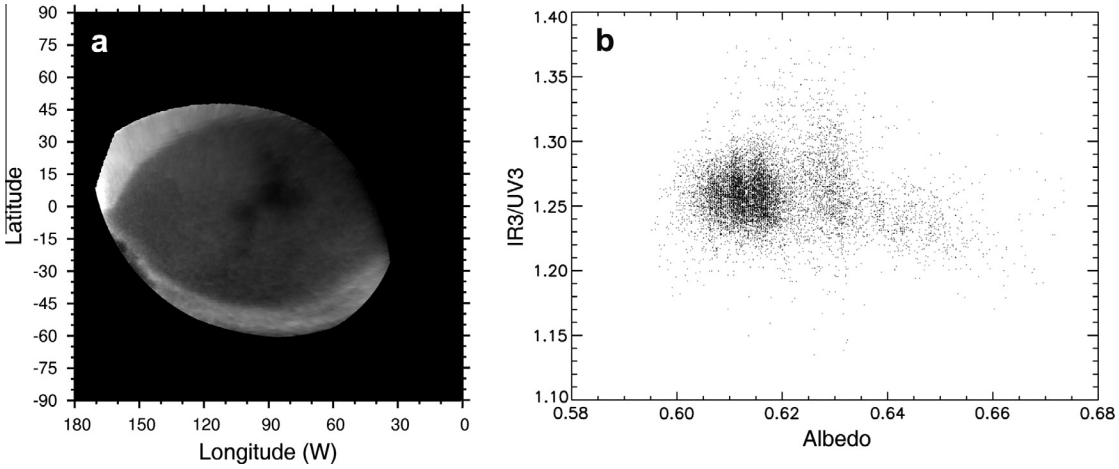

Fig. 11. Albedo and colors of Methone. (a) Broadband visible wavelength (611 nm) albedo map from the May 2012 Cassini flyby. A separate Minnaert photometric correction was applied to each image for normalizing pixel-by-pixel values of albedo at a reference incidence angle of 0° and phase angle of 5°. All of the images were projected to simple-cylindrical map coordinates before merging and were contrast-stretched to show subtle details. The prominent oval-shaped dark region has a mean albedo of 0.61 ± 0.03, including the dark feathery feature near the center that has values as low as 0.60. The bright material surrounding the oval albedo boundary has a mean normal albedo of 0.63 ± 0.01. For details, see Table 4. (b) (CL1:UV3)/(CL1:IR3) ratio of Methone as a function of albedo from two Minnaert-corrected NAC images; N1716192136 (338 nm) and N1716192257 (930 nm).

Table 5
Geometric albedos of embedded satellites from whole-disk phase curves (Hedman et al., 2010).

Satellite	Geometric albedo (611 nm)
Aegaeon	0.25 ± 0.23
Methone	0.57 ± 0.05
Anthe	?
Pallene	0.47 ± 0.11

heavily cratered small satellites. However, the geography of the albedo pattern is suggestive of leading-side thermal anomalies that have been identified on Mimas and Tethys (Howett et al., 2011, 2012). The anomalies in those cases are believed to be produced by preferential bombardment of high-energy electrons on the leading sides of those bodies. However, in those examples, the thermal anomalies coincide with a distinct decrease in IR/UV coloration, which is not detectable in our ISS high-resolution coverage of Methone.

5.6.1. Albedos of arc embedded moons

Hedman et al. (2010) obtained whole-disk, phase-curve measurements of the embedded satellites from Cassini NAC CL1–CL2 filter images at phase angles ($10^\circ < \alpha < 60^\circ$) suitable for estimating whole-disk geometric albedos. However, Pallene was the only one of the Alkyonide satellelites for which a reliable size estimate was available, so that geometric albedos for Aegaeon, Anthe, and Methone could not be determined. Instead the phase curve data were used to estimate the mean radii given the assumption that all of the satellites have the same geometric albedo as Pallene. Now, with our new size estimates (Table 1), we can use Hedman et al.'s measurements to estimate the mean geometric albedos given in Table 5. As in Hedman et al. (2010), these values ignore the opposition effect and are extrapolated to zero phase. The error estimates include a 5% calibration uncertainty in absolute brightness (West et al., 2010) and a contribution from the size estimates in Table 1. It is also assumed that brightness variations due to Cassini's changing viewing perspective average out over the phase curve measurements. While the error bars considerably overlap, the results suggest that the geometric albedos may significantly vary among the embedded satellites.

As yet, there are no reliable size determinations for Anthe. If Anthe has the same geometric albedo as Pallene, then its mean radius would be about 1.1 km (Hedman et al., 2010). Our results suggest that the albedos of the satellites may significantly vary. We note that Hedman's phase curve data was extrapolated from a phase angle range where the opposition surge can be neglected, so Anthe's extrapolated geometric albedo should be no greater than unity, corresponding to a mean radius no less than about 0.75 km. At the other extreme, if its geometric albedo is the same as Aegaeon's ($p_v = 0.25$), then Anthe's mean radius could be on the order of 2.4 km, but could not be much larger because its size in our closest Cassini images would then be greater than a pixel (Table 1).

5.7. Ring/arc-embedded moons: summary

As smooth ellipsoids, the arc/ring embedded moons are unique among well-imaged small Solar System bodies. The smooth surface of Methone suggests some mechanism of fluidizing the regolith on geologic timescales. The mechanism is unknown, as the unique association with rings does not appear to provide an obvious route to sufficiently rapid resurfacing to smooth impact craters. The densities inferred for these objects are low, but not grossly lower than some directly measured values of small satellites and comet nuclei. Whether impacts into very porous regolith can enter a regime where craters are much shallower than expected and ejecta subject to global dispersal is not known, but might be one route to a geologically fluid outer region of the object. These distinctive objects invite work on the impact environment, ring/arc particle amounts and dynamics, the radiation environment, and small-satellite accretion studies.

6. Trojan satellites

Small satellites lie near the leading and trailing Lagrangian points of both Tethys (Telesto and Calypso) and Dione (Helene and Polydeuces). Polydeuces is not well imaged (Table 1); Helene is the best imaged among these at 42 m/pxl, over an object of mean radius of ~18 km. The three well-imaged Trojan satellites all rotate synchronously with their orbital periods as so far observed. The Helene data are good enough (multiple observation times at sufficient resolution) to test for small forced librations. We detect no such rotational librations: the control point solutions have a minimum in residuals consistent with no forced libration (Fig. S3).

For Calypso and Telesto, which have co-orbital libration amplitudes from 25% to 65% the size of Helene's (Oberti and Vienne, 2003; Murray et al., 2005), we obtained sufficiently precise results from a model assuming constant rotation rate. This result obtains mainly because our high-quality observations have insufficient temporal distribution to distinguish among different orientation models.

6.1. Shapes and surface features

Helene has only modest differences between its *a* and *b* axes (Table 1); Telesto and Calypso are much more elongated. The minimum moment orientation calculated from the current shape model of Helene is nearly 20° from the Saturn direction. Significant topographic uncertainty remains in some unilluminated areas (at the time of the last good coverage) in the north of Helene, which may contribute to this result. The slight difference in smallest and intermediate calculated moments means the orientations are not tightly constrained, and thus no inference of inhomogeneity should presently be inferred from the model moment orientation results.

Helene, Calypso and Telesto have large craters, and have widespread filling of craters. Branching patterns of albedo and topography that are somewhat similar to drainage basins (Fig. 12) are evidence of long-range downslope transport. Such evidence of long-range transport is absent on any of the other small saturnian satellites. The surface of a small body most similar to those of the saturnian Trojan satellites is that of Deimos, which shows long range transport over generally smooth surfaces without (except at its south pole) a pattern of collective "drainage." Fig. 10 shows that Helene (and by similar appearances the other Trojans) are distinct from the more lunar-like small satellites and larger bodies whose primary morphologic forms are crater-related.

6.2. High-resolution morphology of Helene

The high-resolution (<50 m/pixel) images of Helene show a surface with few visible sharp craters, some large, smoothed craters, and elongate, tapering darker surfaces that are higher than their immediate surroundings (Fig. 13). Here we designate these as the "upper" (darker) and "lower" (lighter) units. The upper-surface exposures taper downslope and extend up to 8 km from high regions such as degraded large crater rims. The lower unit is brighter (especially in UV; see Section 6.4) and is in most places nearly featureless at the highest resolutions. The darker, upper unit materials form what appear to be residual mesas and pediment-like covers,

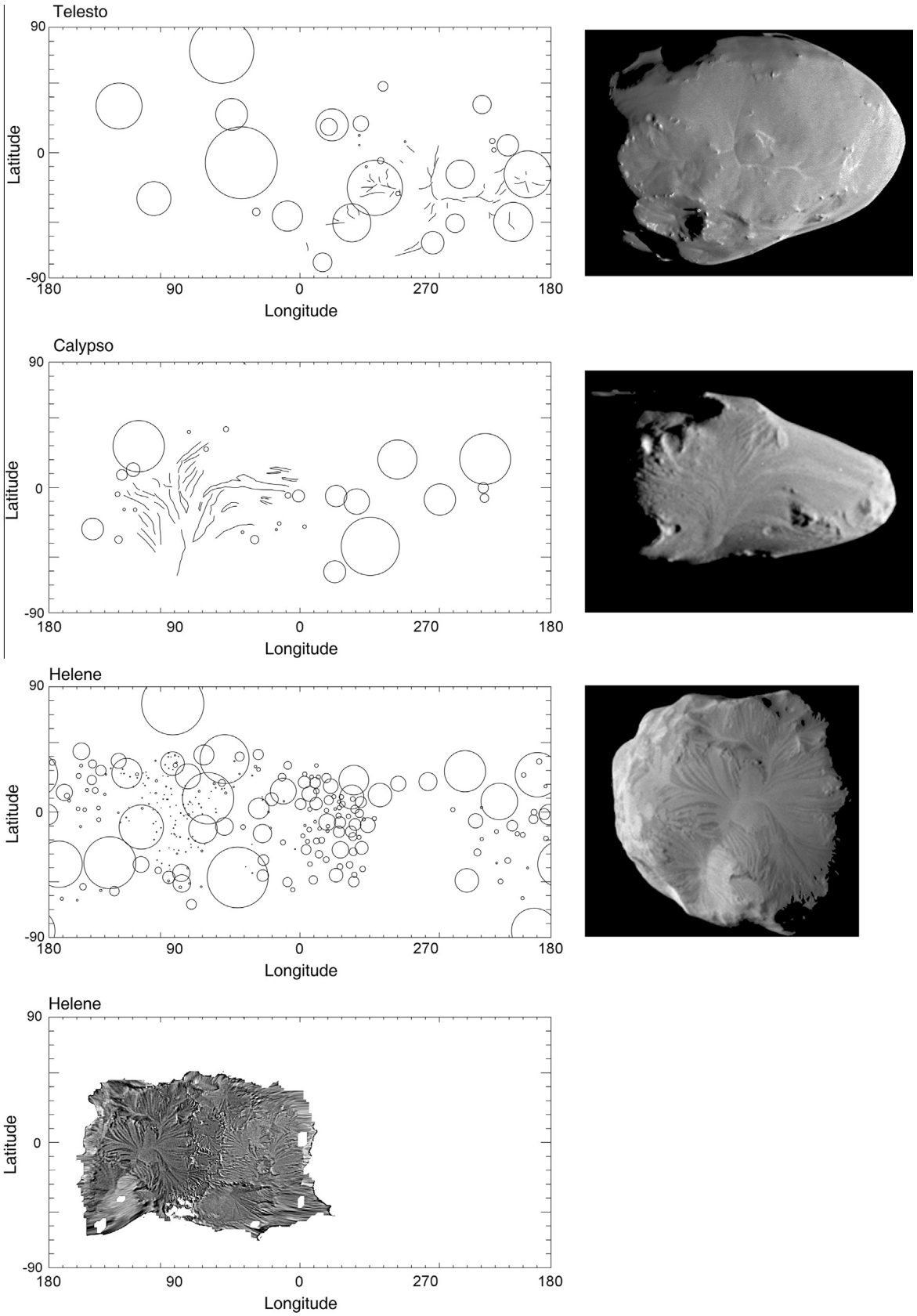

Fig. 12. Maps of Trojan satellites. Simple cylindrical projection. The upper three maps are stylized position plots of craters, the diameters are scaled to body mean radius. Calypso has outlines of the albedo markings added, and Telesto has the "drainage" pattern added. Bottom panel is a map of two UV3-CLR images of Helene high-pass filtered to show its "drainage pattern.".

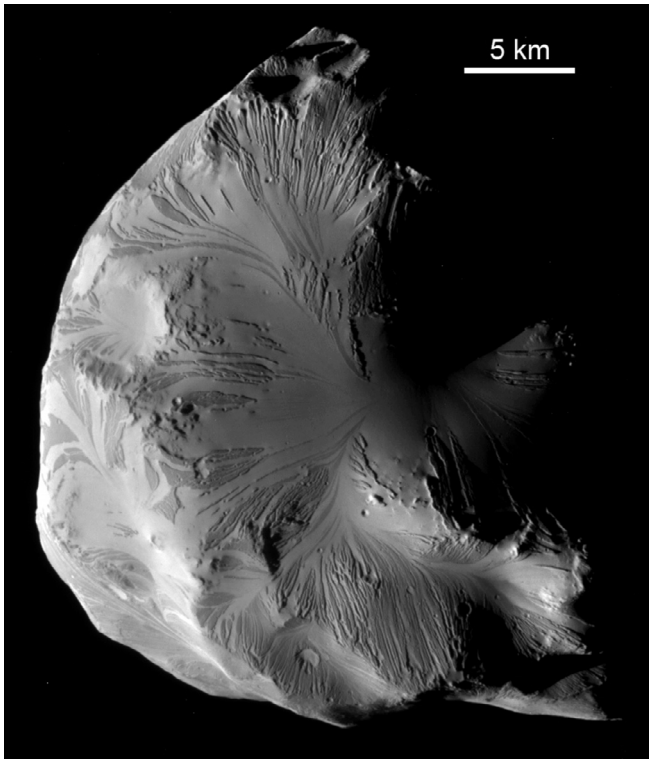

Fig. 13. Best view of Helene. N1687119756, UV3 filter, phase = 97°, sub-spacecraft point is 2.7°N, 124.8°W. North is down in this presentation.

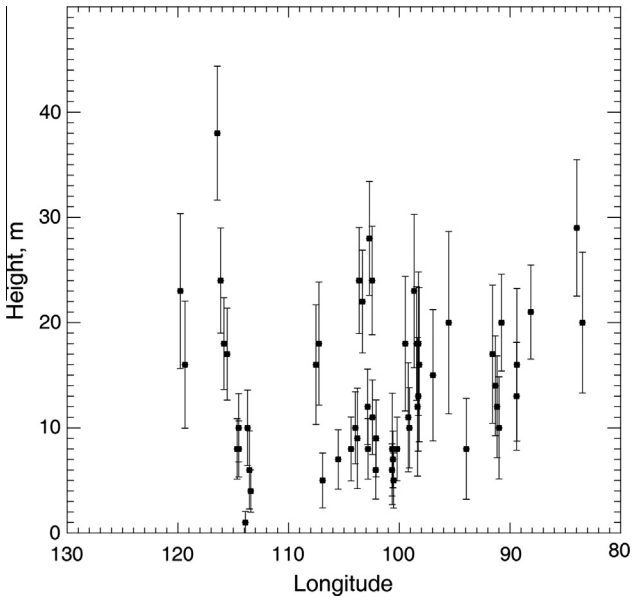

Fig. 14. Heights of scarps bounding upper surface from lower, smooth surface on Helene. Derived from shadow measurements. Error bars are derived by assuming a 1.5 pixel error in shadow length. Abscissa is West longitude.

and show more fine topographic detail at 42+ m/pixel than does the lower unit. This kind of topography is clearly resolved in the region 0–150°W, and is seen at ~110 m/pixel in the region 150–250°W. In the 300–360°W range, observed at ~230 m/pixel, the terrain may be rougher and have higher crater densities at 1–3 km diameter (Section 6.5; Fig. 17a, sub-Saturn vs. Leading side) and may hide thin tapered markings; however, we cannot confidently say whether the upper/lower units are present or absent in this region. The region 250–300°W is poorly observed.

This morphology suggests a covering, apparently widespread if not global, that has or is undergoing erosion at scarps and that is subject to long-distance downslope transport. Because the upper unit is thin, a characteristic immediately apparent from the modest shadow lengths and lack of expression on limb views, it is difficult to get accurate stereogrammetric measure of heights. The shape model of Helene is well enough constrained, however, to use shadow lengths to investigate the heights of the upper unit exposures above the adjacent lower unit. The results are shown in Fig. 14. The average height of the scarps is 15.4 ± 12 m. Given the likely uncertainty in the individual measurements of <5 m, there is almost certainly a real range of scarp heights; the vast majority are under 20 m, and essentially all are under 30 m. These values are consistent with the inability to see any topography on the limb correlating with these forms (42 m/pixel or worse). The height of the scarps might be less than the height of the unit if the lower, smooth materials were filling in around mesas of the upper materials. Given the low slopes on the smooth materials (see Section 6.3), the presence of scarps on topographic divides, and the long downslope extent of roughly the same size and character of scarps, this morphology most likely closely follows the thickness of an actual material unit.

The lower unit provides no thickness fiducials such as partially buried crater rims of known (expected) heights, or erosional exposures of a base. This layer covers large craters, most of which appear far more degraded than anything attributable to a ~20 m cover. The lower unit material thus is probably much thicker than is the upper unit. For estimations of the amounts of materials being moved in this lower unit, we examine the crater densities on the different units and parts of Helene in Section 6.5.

6.3. Comparison of the "drainage patterns" on the Trojan satellites

"Drainage patterns" on the three Trojan satellites are compared in Fig. 15. On Calypso the patterns of elongated light and dark markings are nearly hemispheric in extent; on Telesto they mark relatively smaller, more numerous "drainage basins". The tapering albedo patterns on Calypso (observed at 130 m/pxl) are very similar to those on Helene, and the high-resolution images of the latter are likely a key to both objects. There is some expression of topography in the elongated albedo patterns near the terminator on Calypso, but these are not sufficiently resolved to obtain anything other than crude estimates of relief. Telesto is seen at only modestly worse resolution than Helene (59 vs. 42 m/pxl) and does not replicate the distinct tapering pattern of markings seen on Calypso and Helene. Telesto does clearly have a deep covering of debris also subject to downslope motion, but with a more prominent concentration in branching drainage patterns than on the other Trojan satellites. Rims of the partially filled craters on Telesto are preserved to the extent that blocks are still concentrated on the rims. The material moving into and filling craters is not simply rim material slumping into the craters. This material evidently has much smaller particle sizes and is more widely dispersed than the near-rim ejecta.

Shape models are the basis for evaluating slopes and the amounts of materials in surface units. To calculate slopes, we need a measure or estimate of the body mean density to evaluate the sum of rotational and body-mass accelerations at the surface. We do not have direct mass measurements for these objects. For slopes on Helene this is not a major problem because it has an orbital and rotational period of 2.74 days, so rotational accelerations are small relative to body gravity (rotational accelerations at the sub-Saturn end are ~0.0045 cm s^{-2}). Calypso and Telesto rotate more rapidly; they have 45-h periods that provide modest rotational accelerations, and thus might show more relative effects of self-gravity and rotational acceleration. We have tested

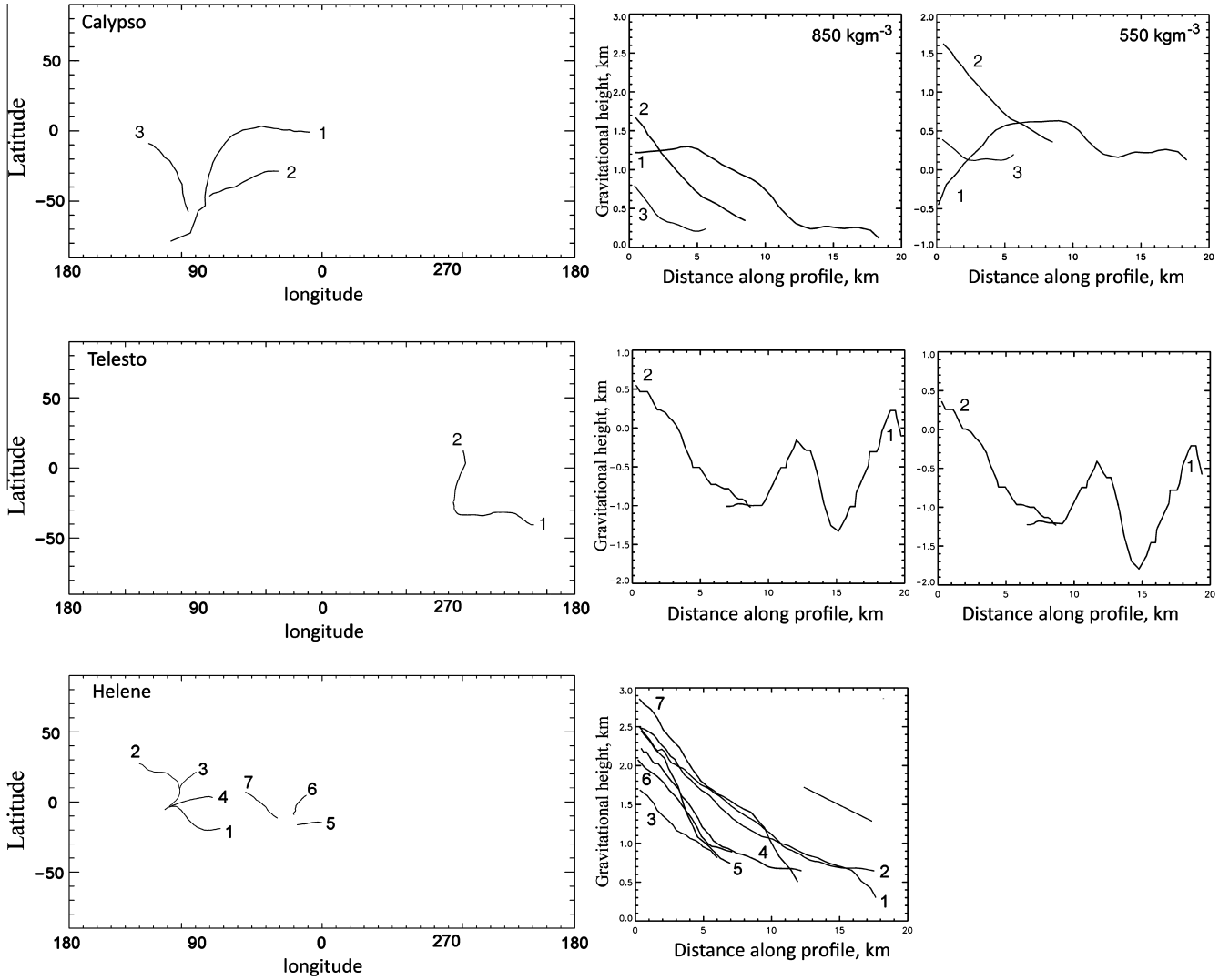

Fig. 15. "Drainage" features on the Trojan satellites. Top row: Calypso drainage map locations; (see Fig. 2B) profiles calculated with mean density of 750 kg m^{-3}; profiles calculated with mean density of 550 kg m^{-3}. Second row: Telesto drainage map locations; profiles for mean density of 750 kg m^{-3}. Slopes on the fill are 10–15°; profiles for assumed mean density of 500 kg m^{-3}. Note the minimal difference in profiles for the two densities. Profile (1) includes two divides. Bottom row: Helene drainage map locations; profiles, density used 750 kg m^{-3}. Reference slope is 5°.

different mean densities for Calypso to see if its slopes are entirely downward along the apparent paths of motion of material for all densities, or if there is a density range where the slope would be the wrong direction or would be interrupted in a manner not consistent with the image interpretation. This comparison is limited by the nature of the smooth areas with elongated markings: stereo solutions are widely spaced across the surface because so few instances of local sharp contrast exist. The results for three "drainage paths" on Calypso for mean densities of 550 and 850 kg m^{-3} are shown in Fig. 15. The path traversing the greatest longitude change (profile 1) is the most sensitive to rotational effects; the results are more plausible for the higher density than for the lower because profiles 1 and 3 are more continuously sloped than for the lower density case. Because of the ~100–150 m uncertainty in the topography along the profiles and possible ambiguities of where a drainage divide might be along the linear markings that suggest flow, we conclude Calypso is probably more dense than the measured small saturnian satellites (Table 1), perhaps greater than 800 kg m^{-3}. However, the considerable uncertainty of this estimate does not affect our conclusion that a deep covering of loose material, likely ejecta, has moved downslope on these objects.

On Helene calculated slopes are not materially affected by the assumed mean density, and we may examine the character of the topography involved in downslope transport. Several paths are plotted in Fig. 15. Slopes along these drainage paths are commonly 6–9°. For comparison, significant downslope transport is observed on 2° slopes on Deimos (Thomas et al., 1996) under roughly similar values of gravity (Deimos is smaller but probably denser than Helene). Of course the materials, and some of the environment, are very different on the two objects.

On Telesto, calculated slopes along the main drainage paths are 10–15° and approach 20° in some places (Fig. 15). The main drainage paths on Telesto do not show diagnostic differences in topography as a function of assumed mean density (Fig. 15). The paths are related to interior morphology of partly-filled/eroded craters, and to other low regions (~thalwegs) between topographic crests that exhibit blocky forms that may be remnants of even larger highly degraded impact craters.

Why are there drainage patterns on these satellites and nothing comparable on other small satellites? More properly put, why are there branching networks of slopes? Cratered landscapes have many radial downslope motion forms, but paths through different craters requires some amount of erosion of rims and depositional

smoothing to allow connections. The different amounts of interconnected surfaces on the satellites range from the lunar-like crater landscapes of Janus and Epimetheus, through the semi-global drainage patterns of the Trojans, to complete smoothing of the arc/ring embedded objects. Further work on the systematics of cratering and ejecta motion in the inner Saturn system may elucidate why the "drainage pattern" result is so unusual.

6.4. Color properties of Trojans and other small satellites

The tapered bright and dark markings on Helene and Calypso (and the less well-defined ones on Telesto) suggest some process-specific surface properties, and invite comparison of the colors to see whether the morphologic diversity is matched by color diversity among the satellites (Morrison et al., 2010). Table 6 gives IR3/UV3 ratios for well-determined areas on several small satellites; this is a partial sampling of the data available for this work's preliminary comparison among objects. Fig. 16 shows IR3/UV3 ratio images for Helene and for Calypso. The upper and lower surface materials on Helene are consistently different colors: the lower unit has a IR3/UV3 value nearly 15% lower than that of the upper surface. On Helene we can resolve the morphology and find unequivocally that surfaces with different geological processes have different color properties. The colors on Telesto have a smaller range than do those on Helene. The IR/UV ratios on Calypso are somewhat higher than those on Helene and have a spread of ratios (s.d. values in Table 6) more similar to those on Helene than on Telesto. Complications include viewing Helene and Calypso on leading sides (see Fig. 12), and the range of phase angles (Table 6).

The colors reported in Table 6 show the trend of bluer (or less red) values moving away from the main rings as noted by Buratti et al. (2010) and Filacchione et al. (2010), due at least in part to the influence of the E-ring particles. The process of E-ring particle impacts (Verbiscer et al., 2007; Kempf et al., 2010) and charged particle bombardment (Johnson et al., 1985; Arridge et al., 2011; Howett et al., 2011, 2012) competes with geological processes, and on some satellites, especially Helene and Calypso, both leave strong signatures. For Helene, the processes of erosion and downslope motion result in a bluer surface; or a less active surface remains/becomes more red. Modeling of the interactions of small and large impacts, charged particles, and the surface motion of materials is left for future attempts to sort out rates of active processes in this system.

The IR3/UV3 color dichotomy is clearly defined on Helene. For the other satellites, local color-contrasts often define boundaries, sometimes distinct and sometimes diffuse or gradational, where redder (high IR3/UV3) features transition to bluer (lower IR3/UV3) ones. On the other satellites we distinguished the color units by incrementally DN-slicing the color ratio images into two color units that best match the spatial pattern of coherent redder and bluer units, respectively. In the separate analysis of Methone (see Section 5.5), the units were defined *a priori* by the segregation of materials shown in the albedo map (Fig. 11). In all other cases, the color units are defined exclusively by the ratio images and are independent of albedo patterns seen in the corresponding original images from which they were constructed. Consequently, any correlation of color unit with albedo is an independent result.

On Helene, Calypso, and Pandora, the spatial distribution of color units is strongly correlated with albedo features: redder materials tend to be darker, and bluer materials tend to be brighter. For the remaining satellites the relationship is less well-defined or indeterminate. In the case of Epimetheus and Methone the range of visible albedos is very small. In our Epimetheus images the small albedo variations can be easily muted by brightness variations due to surface relief. On Janus and Telesto the relationships are non-unique and examples can be found where redder units correspond to locally brighter materials, in addition to the expected relationship

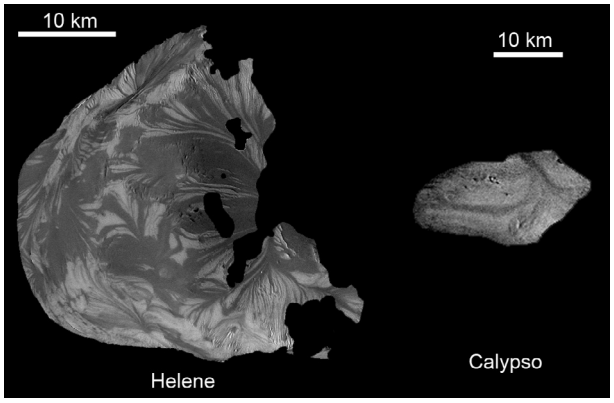

Fig. 16. Patterns of color on Helene and Calypso. Left: IR3/UV3 ratio image, stretched, of Helene images N1687120804 (IR3)/N1687120841 (UV3). Phase angle = 64°; sub spacecraft point (average of pair) 1.5 N, 85.0°W. Upper unit, relatively dark in Fig. 13 (and in IR3 and CLR images) has a higher IR3/UV3 ratio; see Table 6. See Fig. 13 for a UV3 image at higher phase angle. Right: stretched IR3/UV3 ratio image of Calypso images N1644756439 (IR3)/N1644756637 (UV3). Phase angle (average of pair) = 42.4°. For the Helene ratio image, due to its high-resolution and complex shape, systematic changes in color with incidence and emission angles were corrected by applying a separate, wavelength-dependent Minnaert photometric correction to each of the component color images (for IR3, $B_0 = 0.443$, $k = 0.74$, and for UV3, $B_0 = 0.155$, $k = 0.76$). These effects were not significant or were otherwise confined to small areas of the Calypso ratio image.

Table 6
IR3/UV3 color units for the small satellites.

Satellite	IR3/UV3			Phase angle (°)	Images used IR3: UV3
	Bluer	Redder	All		
Ring shepherds					
Prometheus	2.08 ± 0.14	2.41 ± 0.08	2.14 ± 0.18	31	N1640497881: N1640497927
Pandora	1.84 ± 0.12	2.06 ± 0.05	1.85 ± 0.13	54	N1504612418: N1504612385
Co-orbitals					
Janus	1.60 ± 0.05	1.73 ± 0.04	1.68 ± 0.08	58	N1627323305: N1627323227
Epimetheus	1.69 ± 0.04	1.80 ± 0.05	1.76 ± 0.07	65	N1575363199: N1575363109
Alkyonides					
Methone	1.26 ± 0.02	1.26 ± 0.03	1.26 ± 0.02	61	N1716192257: N1716192136
Trojans					
Telesto	1.04 ± 0.02	1.10 ± 0.02	1.06 ± 0.04	58	N1514163666: N1514163600
Helene	1.05 ± 0.06	1.19 ± 0.04	1.09 ± 0.09	64	N1687120804: N1687120841
Calypso	1.20 ± 0.04	1.29 ± 0.05	1.23 ± 0.07	42	N1644756637: N1644756439
	1.26 ± 0.05	1.36 ± 0.04	1.32 ± 0.07	91	N1644754794: N1644754596

in other regions. In many instances imperfections in the shape model can introduce artifacts that mimic albedo patterns in photometrically corrected albedo images. Unresolved differences in subpixel-scale surface relief or roughness can also produce artifacts that appear as dark albedo patches when illuminated at moderate to high incidence angles. However, in some examples, the inverse color-albedo relationship appears to be real, particularly in a few cases where bright crater ejecta correspond to redder material. We may conclude that the colors of small satellite features are probably not uniquely tied to their stratigraphic age.

6.5. Crater densities on Trojans and other small satellites

We use relative (R-plot) and cumulative number/area analysis to compare crater densities (Crater Analysis Working Group 1979). The primary obstacle in crater density analysis on irregularly-shaped objects is the variety of viewing conditions imposed by the different flyby conditions: typically less than one-third the surface is well observed at the closest point of an encounter. Comparisons between objects must allow for different viewing and resolutions. However, there are enough data on several of these objects for revealing comparisons.

Helene is sufficiently well resolved in the best encounter to give information on crater densities on the upper and lower units over nearly a hemisphere. Fig. 17a shows crater densities for different sections of Helene: the best viewed region (0–150°W) at 42–60 m/pixel, which includes the upper surface and lower surface units, a global count of craters with diameters $\gtrsim 2$ km and a section of Helene, between longitudes 310–360°W (labeled "sub-Saturn"), that is seen sufficiently well to count craters >1 km. The larger craters are included in the regional tabulations, but are not included in the two unit counts as both units appear to superpose the large craters.

The combination of R and cumulative plots yield three conclusions. 1: The crater densities superposed on the upper and lower surfaces are indistinguishable from each other, although limited in size range of data. We cannot distinguish ages or crater-retention properties of these units. Because the upper surface may be less disturbed than the lower one which has undergone (or is undergoing) active transport, it conceivably could show a higher crater density, but we cannot really test this possibility because of the small numbers of craters involved. 2: The regional and global tabulations show the fall-off of relative crater densities typical of saturnian satellites at diameters less than ~10 km (Richardson

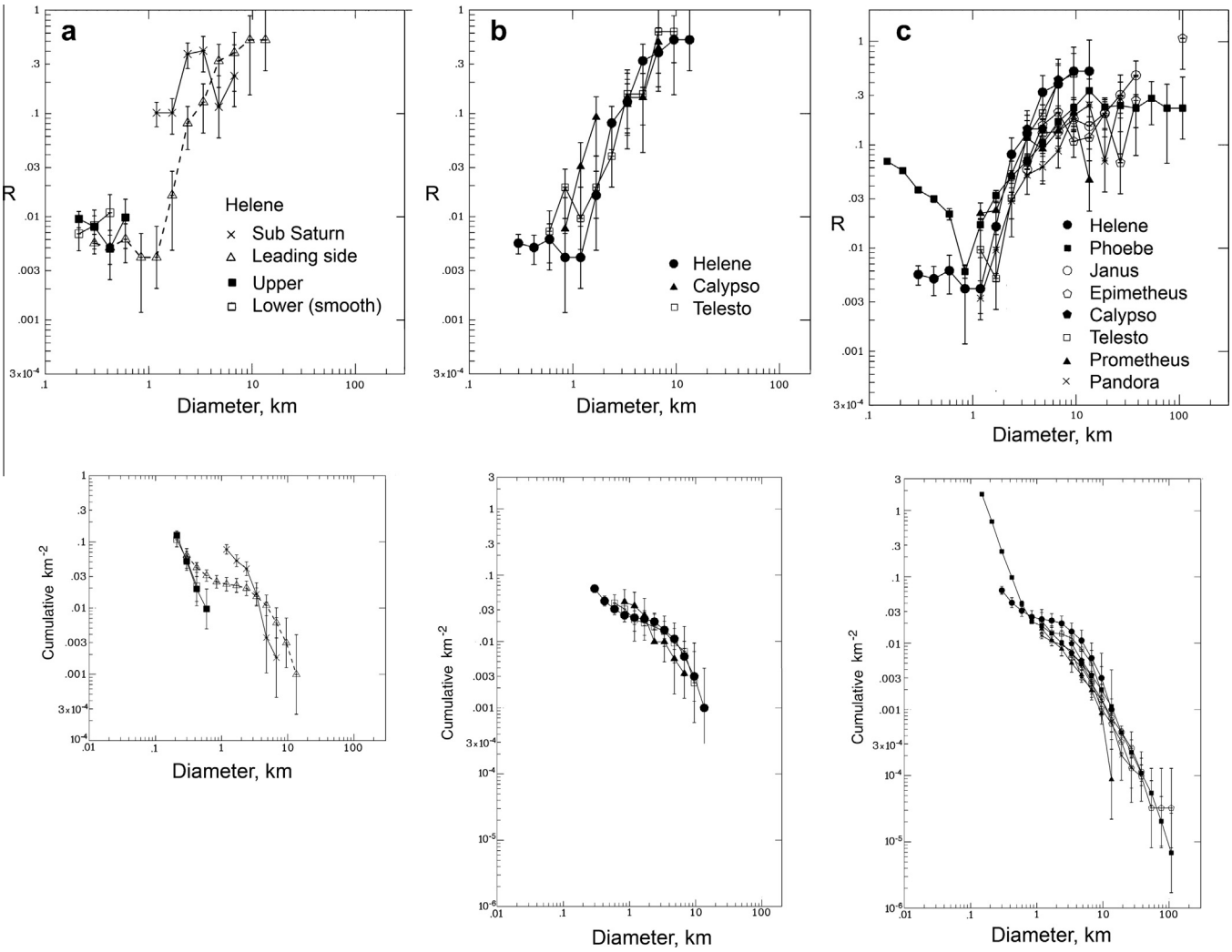

Fig. 17. Crater densities on small saturnian satellites: relative (top panels) and cumulative (lower panels) densities. (a) Regions on Helene: densities of craters on the upper and lower units, and for the entire area (~0–150°W) imaged at high resolution (42–60 m/pixel), sub-Saturn region 300–360°W imaged at 230 m/pixel. Error bars are simply $\sqrt{n}$. (b) Crater densities on Trojan satellites: leading side of Helene, composites of Calypso and Telesto that include best imaged areas and global coverage for largest craters. (c) Crater densities on Helene and composite curves for other small saturnian satellites.

and Thomas, 2010). This has been attributed largely to the impactor size distribution (Richardson and Thomas, 2010). 3: There are real and substantial differences in crater density across the surface of Helene at least at diameters between 0.5 and 3 km.

We now examine point 3 in more detail. The leading side data taken alone have the R-plot fall-off and S-curve shaped cumulative plot that might indicate an impactor size distribution, or a two-stage history where smaller craters were largely obliterated and are now recovering their density. This latter scenario has been a common interpretation on many surfaces and likely is correct in many instances. The sub-Saturn and leading sides have distinctly different densities of craters from 1 to 3 km diameter, and the subset of the leading side in the upper and lower units is distinct from the leading side totals from 0.5 to 0.8 km. No single crater population or episode can cover all three curves. While the leading side curve by itself might indicate one population interrupted by erosion, the difference between the subset of that population and the size distribution in the sub-Saturn area indicates that the same scenario cannot apply to the whole object. Either different areas have different surface processes modifying the crater populations, or areas of different ages were subject to different impacting populations. We cannot choose between these scenarios with the current data.

A comparison of crater densities on the three Trojans is shown in Fig. 17b. The data are from the best viewed portions of all three objects. There is a suggestion that near 1 km diameter Calypso is more densely cratered than Helene, but the large uncertainties from the small number counted means this is only a possibility.

In Fig. 17c, The Helene data are compared to several other small saturnian satellites; the variation shown in Fig. 17b should be kept in mind viewing this plot. Between 1 and 10 km there is some spread of the data with Helene being the most heavily cratered, and Prometheus the least, but differences are marginally significant. Only Phoebe stands out at small sizes, below 700 m diameter, and it is compositionally and orbitally distinct from the other objects that we consider.

6.6. Depths of materials inferred on Helene, Calypso and Telesto

The crater density data do not allow a clear determination that certain sizes of craters on the Trojan satellites have been removed by covering and burial. We thus estimate covering by measurements of dimensions of discrete fill in craters, and by a few depth/diameter measurements.

6.6.1. Discrete fill deposits visible in craters

Degraded craters with definable amounts of filling by the lower unit material help to give estimates of local thicknesses of crater fill on Helene. A 5.6 km crater (−12°, 70°W) has a smooth fill 3.6 km in diameter. If we approximate the crater as a paraboloid of revolution, with height $h = 0.15D$ or $0.3r$, the volume is $(\pi/2) * ha^2$ or $0.059D^3$. The relative volume of the fill is simply $(D_f/D_c)^3$, or 0.25. The volume of the crater is modeled as 10.9 km^3, the fill 2.7 km^3. This fill is assumed to have been gathered from the crater's 25.5 km^2, for a model average depth of 0.11 km. Similarly, a 9.8 km crater (−37°, 174°W) has a flat deposit 3.6 km in diameter, which we model as 2.75 km^3 derived from 75.4 km^2, or an average depth of 0.036 km.

6.6.2. Depths of large craters

We may take the depths of some of the large craters on Helene without discrete fill margins and test if their depths have been reduced by filling. This approach is limited by our relative ignorance of the expected fresh crater depth, and effects of modifications to the crater morphology other than simple filling. There are four well-measured craters with covering by the lower unit 11.5–15 km in diameter in the well-imaged area. These have depth/diameter ratios of 0.12, 0.16, 0.17, and 0.036. Fresh craters on these objects are probably ∼0.15D in depth, although this is a poorly determined ratio for small body craters (Carr et al., 1994; Sullivan et al., 1996; Besse et al., 2012). We simply assume that the three deepest, being close to an expected value of ∼0.15 for depth/diameter, are little affected by filling. We assume the other crater, 11.5 km in diameter and 410 m in depth, has filled from an original depth of $0.15 * 11.5$ km or 1.73 km. The difference in volume, obtained by modeling the crater and subtracting the nominal and modified volumes, is 26 km^3. This material is assumed to have been gathered over the crater's 104 km^2 area, implying an average fill depth of 0.25 km.

6.6.3. Overall estimates for cover on Trojans

In summary, our estimates of the covering on Helene which is the combination of the upper and lower units, include 40–110 m calculated from discrete fill deposit geometry, and up to 250 m calculated from one large crater depth. The discrete fill data are probably the best measurement among these as it is the most direct observation with the fewest assumptions. Thus we make an overall estimate of 40–180 m of cover. This material post-dates most of the 2+ km diameter craters.

On Telesto, a few crater depths may be estimated from stereo and shadows. The estimated average fill depth within these craters is 0.13–0.43 km (Table 7). For Calypso, the covering does not allow estimates of fill within specific craters, and we do not know the size of features that are buried by the widespread debris covering. The topography above the smoother, lineated materials is >200 m, the maximum depths of burial could be greater than this value, but we have no way to restrict these depths.

6.6.4. Predicted ejecta volumes

The role of crater ejecta in any self-covering of these objects depends upon the number of craters and their volumes, the initial distribution of ejecta (whether it lands close to craters or goes into Saturn orbit and is subsequently reaccumulated), and the timing for formation of large craters supplying ejecta relative to formation times of craters or other topography being buried. We can take the visible crater population and estimate ejecta volumes, but we must be aware that the covering and erosion themselves make this a minimum estimate that needs additional context. We take the global crater densities (actually, the most nearly global compilations scaled for the fractional area involved) and simply apply the above approximation of crater volume of $V = 0.059D^3$ (on the low-gravity objects, all craters should be simple) to obtain estimates given in Table 8.

Any two of the four largest craters on Helene could supply a global covering of ∼50 m. In the high-resolution images the upper and lower units post-date the larger craters, but there are large craters seen at longitudes outside the 0–150°W range of the high-resolution coverage that could supply this amount of material, but because of much lower resolution, the stratigraphic relation of the craters in this region to the covering cannot be established.

Table 7
Estimated crater fill on Telesto.

Diam.	Depth	Dimensions, km		Fill	Average fill
		Nominal depth	Max.		
Dimensions, km					
6.4	0.6	1–1.3	0.4	0.7	0.13–0.23
8.9	0.5	1.3–1.8	0.8	1.3	0.26–0.43
7.1	0.4	1.1–1.4	0.7	1.0	0.23–0.33

Nominal depth with d/D of 0.15–0.20.

Table 8
Predicted ejecta on selected satellites.

Object	Total area, (km^2)	Count area (km^2)	Vol. (km^3)	Depth (km)	Depth (R_m)
Helene	4380	3810	1140	0.30	0.017
Calypso	1310	910	87	0.10	0.01
Telesto	2075	1600	310	0.19	0.016
Janus	104090	99540	50020	0.50	0.006
Epimetheus	44760	42570	11800[a]	0.28	0.005
			61600	1.45	0.025
Phoebe	147000	147000	241000	1.7	0.016

[a] Value excludes south polar depression.

Although we cannot rule out Helene being self-covered, the distinct appearance of these covering units on Helene and Calypso suggests different processes or histories from the large-scale cratering, covering, and gardening seen on other well-imaged objects. Additionally, the geographical variation in crater densities (Section 6.5) on Helene suggests effects other than build-up of randomly distributed cratering.

For comparison, the satellite best known for a nearly global, smooth covering by likely ejecta is Deimos. The latter object may have achieved its appearance from an ~80 m cover of ejecta coming from a single, large crater. The estimated ejecta depth over this 6 km radius object is only $0.013R_m$, on the order of those values in Table 8. The south polar 94 km depression on Epimetheus, if counted as a crater, completely dominates the calculated ejecta (Table 8), yet the surface within that crater is old enough to have accumulated a large population of craters. Deimos's large crater (~7.5 km diameter) is young enough that only a modest population of superposed craters exists, in addition to some craters apparently buried and re-exposed by downslope motion of the accumulated ejecta (Thomas, 1998). Deimos's radically different appearance from that of Epimetheus may arise simply because of the different relative timing of the largest cratering events.1

6.7. Interpretations of surfaces of Trojan satellites

While we cannot rule out craters on Helene providing its covering materials, global distribution of ejecta is not what is expected. The dominance of gravity scaling of craters even on small (but weak) objects (Asphaug and Melosh, 1993; Richardson, 2009) should leave most ejecta concentrated near the source crater. The detailed information available on the martian satellites supports the prediction (Thomas, 1998) that most ejecta landed near large source craters: both near Stickney (D = 9.4 km; Phobos R_m = 11.1 km) on Phobos and near the unnamed ~9 km crater on Deimos (R_m = 6.2 km). Both require large radial variations in ejecta thicknesses. The upper layer on Helene (Fig. 14) shows no organized pattern in thickness. Initial truly global distribution of ejecta on Helene (really escaped and recaptured ejecta) would probably require very high-strength materials that foster higher velocity ejecta than would be generated by cratering in a largely gravity-scaling environment. The high inferred porosities of these objects is an indication that high-strength materials do not have a role in cratering on these bodies.

Apart from material properties, the distinction of the Trojan satellite appearances may be the dynamical position. The dynamical positions could be important if the associated large satellites, Tethys and Dione, could supply materials for accretion onto the Trojans that are not available to satellites such as Janus, Epimetheus, Phoebe or others. This scenario of course requires escape of ejecta from a much deeper gravity well than the Trojans have. The offsetting factor would be the relative areas of Tethys and Dione compared to the Trojans and the very large craters that can occur on those surfaces. Dione has ~900 times the area of Helene, so a 100 m cover on Helene would correspond to the volume of an 11 cm cover on Dione. Tethys has ~2700 times the area of Calypso, so a 100 m layer on Calypso is equivalent to a ~37 cm cover on Tethys. For Helene the required volume is ~200–800 km^3 (40–180 m over an area of 4390 km^2 from the shape model).

Exchange of ejecta among satellites in the Saturn system and specifically Tethys and its Trojans has been modeled by Alvarellos et al. (2005) and Dobrovolskis et al. (2009). Large impacts into Tethys such as Odysseus (440 km diameter, leading side) and Penelope (180 km diameter, trailing side) were taken as sources of ejecta. Although a large fraction of the escaping material could in principle reach the Lagrangian points, only 0.1% intersects the small cross sections of these moons. The simulations did not include oblique impacts, jetting, or radiative or magnetospheric effects on small particles. Because escaping, high-velocity ejecta will assume semi major axes different from the source body, ejecta from Tethys can reach Enceladus and Dione. Thus, it might be expected that covering on Tethys's Trojans might have a significant component originating from Dione, and Helene might acquire debris from Tethys. Both Dione and Tethys have at least five craters >100 km diameter, with ejecta volumes >15,000 km^3 each, assuming 2 km of excavation. We conclude that more specific modeling of the large crater histories on Tethys and Dione are needed to test whether there would be enough ejecta in their orbits for a long enough time for the Trojans to pick up sufficient ejecta from the outside to distinguish their appearance from other small satellites that do not share orbits with much larger objects that might be sources of external ejecta.

7. Overall properties of the small satellites

Albedo and colors of the small satellites show trends with distance from Saturn, and surface morphology varies with dynamical position. The mean densities also show a radial trend (Fig. 18a), but one that would appear to peak with the co-orbitals. However, their densities as a function of mean radius, thus as something of a function of internal pressures, also show some correlation (Fig. 18b). The central pressures in all of these objects are low compared to the medium-sized moons where compaction might play some role (Eluszkiewicz, 1990). On such low-density, low-pressure objects, dynamical pressures associated with impacts might be suspected of a role in determining porosities, but the smooth surfaces of Methone and Pallene make such speculation dubious. Modeling of the evolution of all these bodies is at an early stage, but Cassini has now provided more constraints on such inquiries.

8. Summary

The surface features of the inner small satellites of Saturn are specific to the dynamical environment each satellite occupies (Table 9). Satellites within the main rings, embedded within ring arcs, or in Trojan orbits display a variety of depositional modifications. The F-ring shepherds and the co-orbitals display more

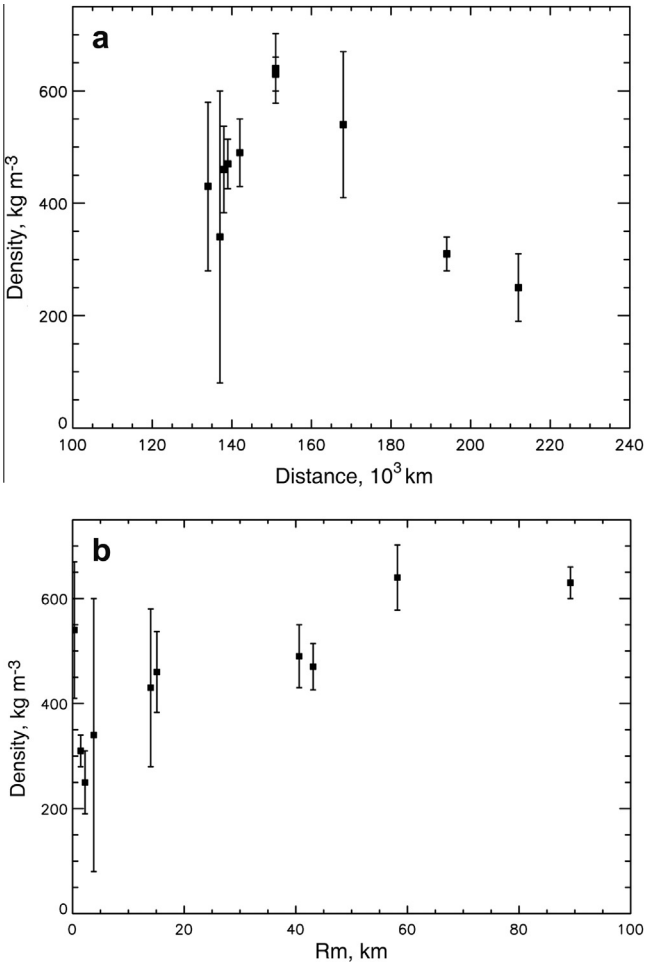

Fig. 18. Mean density of inner small satellites. (a) As function of distance from Saturn. (b) As function of satellite mean radius.

Table 9
Morphologic characteristics of Saturn inner small satellites.

Within main rings	Pan	Equatorial ridge
	Daphnis	Equatorial ridge?
	Atlas	Equatorial ridge
F-ring shepherds	Prometheus	Stripped core? Cratered
	Pandora	Cratered, grooves
Co-orbital	Epimetheus	Cratered, grooves
	Janus	Cratered
Arc, diffuse ring	Aegaeon	Ellipsoid
	Methone	Smooth ellipsoid
	Anthe	?
	Pallene	Smooth ellipsoid
Trojan	Telesto	Deep crater fill, downslope transport
	Calypso	Deep fill, global downslope transport
	Polydeuces	?
	Helene	Global deposition, backwasting, downslope transport

heavily cratered surfaces, more evidence of internal structural features, and minimal depositional materials. The arc-embedded moons are likely near-equilibrium forms and have low densities, with implied porosities reaching ~65%. The combination of surface features correlated with dynamical position, and the presence of significant depositional forms, suggests ongoing processes in the inner Saturn system able to compete with cratering modifications of surfaces. We confirm that photometric and color properties for many of these small satellites are dependent on distance from Saturn. From Atlas to the Trojans albedos generally increase and colors become bluer (Buratti et al., 2010) likely showing the influence of E-ring particles, whose eventual source is Enceladus (Verbiscer et al., 2007). Spectrally these satellite surfaces all appear to be water ice with minimal contaminants that are distinct from those in the darker components of regoliths of outer satellites such as Iapetus, Phoebe or Hyperion (Buratti et al., 2010; Filacchione et al., 2010). Although albedo and colors show radial trends from Saturn, local geology, such as downslope transport, also affects color properties and may indicate relative rates of different processes.

One of the primary lessons of this study is how little we know of the processes that move material around on low-gravity surfaces. We do not know how arc/ring embedded moons are smoothed, nor if they relate to smoothing on objects such as Atlas. We do not know how the "drainage basin" patterns on the Trojan moons are established and modified. We do not know how the sharp albedo boundary on Methone is generated or maintained. In short, elucidating the competing regolith processes on these bodies has barely started.

Acknowledgments

Funded in part by the Cassini Project. We thank T. Ansty, B. Carcich, K. Consroe, T. Denk, R. Rich Goldweber, C. Jackman, J. Joseph, T. Shannon, P. Smith, D. Wilcox for technical help. Reviews by J. Spitale and an anonymous reviewer helped strengthen the paper's presentation.

Appendix A. Supplementary material

Supplementary data associated with this article can be found, in the online version, at http://dx.doi.org/10.1016/j.icarus.2013.07.022.

References

Alvarellos, J.L., Zahnle, K.J., Dobrovolskis, A.R., Hamill, P., 2005. Fates of satellite ejecta in the Saturn system. Icarus 178, 104–123.
Archinal, B.A. et al., 2011. Report of the IAU working group on cartographic coordinates and rotational elements: 2009. Celest. Mech. Dyn. Astron. 109, 101–135.
Arridge, C.S. et al., 2011. Mapping magnetospheric equatorial regions at Saturn from Cassini Prime Mission Observations. Space Sci. Rev. 164, 1–83.
Asphaug, E., Melosh, H.J., 1993. The Stickney impact of Phobos - A dynamical model. Icarus 101, 144–164.
Barnouin-Jha et al., 2008. Small-scale topography of 25143 Itokawa from the Hayabusa laser altimeter. Icarus 198, 108–124.
Benner, L.A.M. et al., 2012. Arecibo and goldstone radar observations of binary near-Earth asteroid and marco Polo-R Mission Target (175706) 1996 FG3. AAS/Division for Planetary Sciences Meeting 44. Abstracts #102.06.
Besse, S., Lamy, P., Jorda, L., Marchi, S., Barbieri, C., 2012. Identification and physical properties of craters on Asteroid (2867) Steins. Icarus 221, 1119–1129.
Brownlee, D.E. et al., 2004. The surface of young Jupiter family Comet Wild 2: View from the Stardust spacecraft. Science 304, 1764–1769.
Brozovic, M. et al., 2010. Radar images and shape model of a triple Asteroid (136617) 1994CC. Bull. Am. Astron. Soc. 42, 1080.
Brozovic, M. et al., 2011. Radar and optical observations and physical modeling of triple near-Earth Asteroid (136617) 1994 CC. Icarus 216, 241–256.
Buratti, B.J. et al., 2010. Cassini spectra and photometry 0.25–5.1 μm of the small inner satellites of Saturn. Icarus 206, 524–536.
Burns, J.A. et al., 2004. Jupiter's ring-moon system. In: Bagenal, F., Diwling, T.E., McKinnon, W.B. (Eds.), Jupiter: The Planet, Satellites, and Magnetosphere. Cambridge Univ. Press, pp. 241–262.
Busch, M.W. et al., 2011. Radar observations and the shape of near-Earth Asteroid 2008 EV5. Icarus 212, 649–660.
Carr, M.H., Kirk, R.L., McEwen, A., Veverka, J., Thomas, P., Head, J.W., Murchie, S., 1994. The geology of Gaspra. Icarus 107, 61–71.

Castillo-Rogez, J.C., Johnson, T.V., Thomas, P.C., Choukroun, M., Matson, D.L., Lunine, J.I., 2012. Geophysical evolution of Saturn's satellite Phoebe, a large planetesimal in the outer Solar System. Icarus 219, 86–109.
Chandrasekhar, S., 1969. Ellipsoidal Figures of Equilibrium. Yale Univ. Press, New Haven.
Charnoz, S., Brahic, A., Thomas, P.C., Porco, C.C., 2007. The equatorial ridges of Pan and Atlas: Terminal accretionary ornaments? Science 318, 1622–1624.
Denk, T., Mottola, S., Roatsch, T., Rosenberg, H., Neukum, G., 2011. Rotation periods of irregular satellites of Saturn. EPSC-DPS Joint Meet. Abstract #1452.
Dermott, S.F., 1979. Shapes and gravitational moments of satellites and asteroids. Icarus 37, 575–586.
Dermott, S.F., Murray, C.D., 1981a. The dynamics of tadpole and horseshoe orbits. I – Theory. Icarus 48, 1–11.
Dermott, S.F., Murray, C.D., 1981b. The dynamics of tadpole and horseshoe orbits II. The coorbital satellites of Saturn. Icarus 48, 12–22.
Dermott, S.F., Thomas, P.C., 1988. The shape and internal structure of Mimas. Icarus 73, 25–65.
Dobrovolskis, A.R., Burns, J.A., 1980. Life near the Roche limit – Behavior of ejecta from satellites close to planets. Icarus 42, 422–441.
Dobrovolskis, A.R., Alvarellos, J.L., Zahnle, K.J., Lissauer, J.J., 2009. Fates of ejecta from co-orbital satellites: Tethys, Telesto, and Calypso. AGU (Fall Meet.). Abstracts 1146.
Dones, L., Chapman, C.R., McKinnon, W.B., 2009. Icy satellites of Saturn: Impact cratering and age determination. In: Saturn from Cassini–Hyugens. Springer, pp. 613–635.
Eluszkiewicz, J., 1990. Compaction and internal structure of Mimas. Icarus 84, 215–225.
Filacchione, G. et al., 2010. Saturn's icy satellites investigated by Cassini–VIMS. II. Results at the end of nominal mission. Icarus 206, 507–523.
Fujiwara, A. et al., 2006. The rubble-pile Asteroid Itokawa as observed by Hayabusa. Science 312, 1330–1334.
Gladman, B. et al., 2001. Discovery of 12 satellites of Saturn exhibiting orbital clustering. Nature 412, 163–166.
Harris, A.W., Fahnestock, E.G., Pravec, P., 2009. On the shapes and spins of "rubble pile" asteroids. Icarus 199, 310–318.
Hedman, M.M. et al., 2007. The source of Saturn's G ring. Science 317, 653–656.
Hedman, M.M., Murray, C.D., Cooper, N.J., Tiscareno, M.S., Beurle, K., Evans, M.W., Burns, J.A., 2009. Three tenuous rings/arcs for three tiny moons. Icarus 199, 378–386.
Hedman, M.M., Cooper, L.J., Murray, C.D., Beurle, K., Evans, M.W., Tiscareno, M.S., Burns, J.A., 2010. Aegaeon (Saturn LIII), a G-ring object. Icarus 207, 433–447.
Helfenstein, P., Hillier, J., Veverka, J., Moersch, J., Weitz, C., 1989. Uranus satellites: Albedo and color maps from Voyager imaging. Lunar Planet. Sci. 20, 402–403 (abstract).
Helfenstein, P. et al., 1994. Galileo photometry of Asteroid 951 Gaspra. Icarus 107, 37–60.
Hirata, N., Miyamoto, H., 2012. Dust levitation as a major resurfacing process on the surface of a saturnian icy satellite, Atlas. Icarus 220, 106–113.
Holsapple, K.A., 2001. Equilibrium configurations of solid cohesionless bodies. Icarus 154, 432–448.
Holsapple, K.A., 2004. Equilibrium figures of spinning bodies with self-gravity. Icarus 172, 272–303.
Holsapple, K.A., Michel, P., 2008. Tidal disruptions. II. A continuum theory for solid bodies with strength, with applications to the Solar System. Icarus 193, 283–301.
Howard, A.D., Moore, J.M., Schenk, P.M., White, O.L., Spencer, J., 2012. Sublimation-driven erosion on Hyperion: Topographic analysis and landform simulation model tests. Icarus 220, 268–276.
Howett, C., Spencer, J.R.J., Schenk, P., Johnson, R.E., Paranicas, C., Hurford, T., Verbiscer, A., Segura, M., 2011. A high-amplitude thermal inertia anomaly of probable magnetospheric origin on Saturn's moon Mimas. Icarus 216, 221–226.
Howett, C.J.A., Spencer, J.R., Hurford, T., Verbiscer, A., Segura, M., 2012. PacMan returns: An electron-generated thermal anomaly on Tethys. Icarus 221, 1084–1088.
Jacobson, R.A. et al., 2006. The gravitational field of Saturn and the masses of its major satellites. Astron. J. 132, 2520–2526.
Jacobson, R.A. et al., 2008. Revised orbits of Saturn's small inner satellites. Astron. J. 135, 261–263.
Johnson, R.E. et al., 1985. Charged particle modification of ices in the saturnian and jovian systems (in ices in the Solar System). NATO ASI Ser. 156, 301–315.
Johnson, T.V., Castillo-Rogez, J.C., Matson, D.L., Thomas, P.C., 2009. Phoebe's shape: Possible constraints on internal structure and origin. Lunar Planet. Sci. 40. Abstract #2334.
Keller, H.U. et al., 2010. E-type Asteroid (2867) Steins as imaged by OSIRIS on board Rosetta. Science 327, 190–193.
Kempf, S., Beckmann, U., Schmidt, J., 2010. How the Enceladus dust plume feeds Saturn's E ring. Icarus 206, 446–457.
Minnaert, M., 1941. The reciprocity principle of linear photometry. Astrophys. J. 93, 403–410.
Morrison, S.J., Thomas, P.C., Tiscareno, M.S., Burns, J.A., Veverka, J., 2009. Grooves on small saturnian satellites and other objects: Characteristics and significance. Icarus 204, 262–270.
Morrison, S.J., Helfenstein, P., Thomas, P.C., Veverka, J., 2010. Color photometry of the small saturnian satellites: Global and regional variations on Prometheus and Calypso. Bull. Am. Astron. Soc. 42, 955.
Murray, C.D., Cooper, N.J., Evans, M.W., Beurle, K., 2005. S/2004 S5: A new co-orbital companion for Dione. Icarus 179, 222–234.
Nolan, M.C. et al., 2012. The shape of OSIRIS-REx mission target 1999 RQ36 from radar and lightcurve data. LPI Contrib. 1667, 6345.
Noyelles, B., 2010. Theory of the rotation of Janus and Epimetheus. Icarus 207, 887–902.
Oberti, P., Vienne, A., 2003. An upgraded theory for Helene, Telesto, and Calypso. Astron. Astrophys. 397, 353–359.
Ostro, S.J. et al., 2006. Radar imaging of binary near-Earth Asteroid (66391) 1999 KW4. Science 314, 1276–1280.
Owen Jr., W.M., 2003. Cassini ISS geometric calibration. JPL Interoffice Memorandum 312 (E-2003-001).
Porco, C.C. et al., 2004. Cassini Imaging Science: Instrument characteristics and anticipated scientific investigations at Saturn. Space Sci. Rev. 115, 363–497.
Porco, C.C. et al., 2005. Cassini Imaging Science: Initial results on Phoebe and Iapetus. Science 307, 1237–1242.
Porco, C.C., Thomas, P.C., Weiss, J.W., Richardson, D.C., 2007. Saturn's small inner satellites: Clues to their origins. Science 318, 1602–1607.
Richardson, J.E., 2009. Cratering saturation and equilibrium: A new model looks at an old problem. Icarus 204, 697–715.
Richardson, J.E., Melosh, H.J., 2013. An examination of the Deep Impact collision site on Comet Tempel 1 via Stardust-NExT: Placing further constraints on cometary surface properties. Icarus 222, 492–501.
Richardson, J.E., Thomas, P.C., 2010. Uncovering the saturnian impactor population via small satellite cratering records. Lunar Planet. Sci. 41. Abstracts 1523.
Richardson, D.C., Elankumaran, C.P., Sanderson, R.E., 2005. Numerical experiments with rubble piles: Equilibrium shapes and spins. Icarus 173, 349–361.
Robinson, M.S., Thomas, P.C., Veverka, J., Murchie, S., Carcich, B., 2001. The nature of ponded deposits on Eros. Nature 413, 396–400.
Robutel, P., Rambaux, N., Castillo-Rogez, J., 2011a. Analytical description of physical librations of saturnian coorbital satellites Janus and Epimetheus. Icarus 211, 758–769.
Robutel, P., Rambaux, N., El Moutamid, M., 2011. Influence of the coorbital resonance on the rotation of the Trojan satellites of Saturn. arXiv:1111.1076 (e-prints).
Roussos, E. et al., 2008. Energetic electron signatures of Saturn's smaller moons: Evidence of an arc of material at Methone. Icarus 193, 455–464.
Russell, C.T. et al., 2012. Dawn at Vesta: Testing the protoplanetary paradigm. Science 336, 684–686.
Sharma, I., 2009. The equilibrium of rubble-pile satellites: The Darwin and Roche ellipsoids for gravitationally held granular aggregates. Icarus 200, 636–654.
Sharma, I., 2013. Structural stability of rubble-pile asteroids. Icarus 223, 367–382.
Sharma, I., Jenkins, J.T., Burns, J.A., 2009. Dynamical passage to approximate equilibrium shapes for spinning, gravitating rubble asteroids. Icarus 200, 304–322.
Simonelli, D.P., Thomas, P.C., Carcich, B.T., Veverka, J., 1993. The generation and use of numerical shape models for irregular Solar System objects. Icarus 103, 49–61.
Sullivan, R. et al., 1996. Geology of 243 Ida. Icarus 120, 119–139.
Sullivan, R., Anderson, R., Biesiadecki, J., Bond, T., Stewart, H., 2011. Cohesions, friction angles, and other physical properties of martian regolith from Mars Exploration Rover wheel trenches and wheel scuffs. J. Geophys. Res. (Planets) 116, 2006. http://dx.doi.org/10.1029/2010JE003625.
Thomas, P., 1989. Shapes of small satellites. Icarus 77, 248–274.
Thomas, P.C., 1993. Gravity, tides, and topography on small satellites and asteroids – Application to surface features of the martian satellites. Icarus 105, 326–334.
Thomas, P.C., 1998. Ejecta emplacement on the martian satellites. Icarus 131, 78–106.
Thomas, P.C., 2010. Sizes, shapes, and derived properties of the saturnian satellites after the Cassini nominal mission. Icarus 208, 395–401.
Thomas, P.C., Adinolfi, D., Helfenstein, P., Simonelli, D., Veverka, J., 1996. The surface of Deimos: Contribution of materials and processes to its unique appearance. Icarus 123, 536–556.
Thomas, P.C. et al., 2002. Eros: Shape, Topography, and Slope Processes. Icarus 155, 18–37.
Thomas, P.C. et al., 2007a. Shapes of the saturnian icy satellites and their significance. Icarus 190, 573–584.
Thomas, P.C. et al., 2007b. Hyperion's sponge-like appearance. Nature 448, 50–56.
Tiscareno, M.S., Thomas, P.C., Burns, J.A., 2009. The rotation of Janus and Epimetheus. Icarus 204, 254–261.
Vanicek, P., Krakiwsky, E.J., 1986. Geodesy: The Concepts, second ed. Elsevier, New York.
Verbiscer, A., French, R., Showalter, M., Helfenstein, P., 2007. Enceladus: Cosmic graffiti artist caught in the act. Science 315, 815.
Veverka, J. et al., 2013. Return to Comet Tempel 1: Overview of Stardust-NExT results. Icarus 222, 424–435.
West, R. et al., 2010. In-flight calibration of the Cassini imaging science sub-system cameras. Planet. Space Sci. 58, 1475–1488.
Yoder, C.F., Synnott, S.P., Salo, H., 1989. Orbits and masses of Saturn's co-orbiting satellites, Janus and Epimetheus. Astron. J. 98, 1875–1889.